Title: Minimal determinants for durable B cell antibody response towards virus-like antigens

Authors: Wei-Yun Wholey[1†], Alexander R. Meyer[1†], Sekou-Tidiane Yoda[1], Bryce Chackerian[2], Julie Zikherman*[3], Wei Cheng[1,4]*

Affiliations:

[1]*Department of Pharmaceutical Sciences, 428 Church Street, University of Michigan, Ann Arbor, Michigan 48109, USA*

[2]*Department of Molecular Genetics and Microbiology, School of Medicine, University of New Mexico, Albuquerque, New Mexico 87131, USA*

[3]*Division of Rheumatology, Rosalind Russell and Ephraim P. Engleman Rheumatology Research Center, Department of Medicine, University of California, San Francisco, California 94143 USA*

[4]*Department of Biological Chemistry, 1150 W. Medical Center Dr., University of Michigan Medical School, Ann Arbor, Michigan 48109, USA*

*Corresponding authors:

Dr Julie Zikherman
513 Parnassus Avenue
Room HSW1201E, Box 0795
San Francisco, CA, 94143-0795
Tel: (415)-476-1689
email address: julie.zikherman@ucsf.edu

Dr Wei Cheng
University of Michigan
428 Church Street
Ann Arbor, MI, 48109-1065
Tel: (734) 763-3709
Fax: (734) 615-6162

email address: chengwe@umich.edu

Keywords: antibody, virus-like structures, epitope density, nucleic acids, Toll-like receptor, virus-like particles

†: Both authors contributed equally to this work.

Abstract:

Virus-like particles are known to induce long-term humoral immunity, but the mechanisms involved have been less understood. Model antigens (Ags) are indispensable for understanding B-cell responses to immunization but immunogens that facilitate the dissection of viral features on B-cell responses are limited. Here we describe a system of liposome-based virus-like structures that allowed us to independently vary the contributions of fundamental viral attributes to the initiation and durability of antibody (Ab) responses, and to do so without additional adjuvants. We show that Ag display on a virion-sized liposome can serve as a stand-alone danger signal to initiate class-switched Ab response in the absence of either T cell help or Toll-like receptors but requires CD19. Introduction of internal nucleic acids lowers the epitope density required to elicit a response and transforms these structures into highly potent immunogens that are independent of CD19 engagement and rival well-established bacteriophage virus-like particles in the resulting Ag-specific IgG titers. As early as day 5 after injection, structures decorated with even a few molecules of surface Ag at doses as low as 100 ng can induce all IgG subclasses of Ab characterized by an off rate of ~0.0005 s^{-1}. A single injection of these structures at low Ag dose led to life-long neutralizing Ab production in BALB/c mice. Thus, Ag valency and intrinsic sensing of viral nucleic acids coordinate quantitatively to mediate long-lasting antiviral IgG in a primary immune response.

One-sentence summary:

Reconstitution of minimal viral signals necessary to trigger durable antiviral IgG

Introduction

Two biophysical attributes shared by most animal viruses are the surface display of virus-specific proteins at certain densities and the encapsulation of a viral nucleic acid genome inside the virion. Naturally occurring virions have densities of surface proteins that vary over several orders of magnitude, ranging from 200 to 30,000 molecules per μm^2 (*1, 2*). From the perspective of the host, a threshold density of viral surface proteins may be critical for the recognition by germline B cell Ag receptors (BCRs) to efficiently trigger humoral responses (*3*). In fact, Ag valency has profound effects on both the magnitude of B cell responses and B cell fate *in vivo* (*4*) and it is well established that a high-density, ordered display of an epitope on virus-like particles can elicit strong Ab responses and even break B cell tolerance (*5-12*). In addition, the encapsulated nucleic acid (NA) inside virions can activate endosomal NA-sensing Toll-like Receptors (TLRs) (*13*) after BCR-mediated endocytosis, and produce a cascade of downstream effects on B cells (*14-18*). It has been well established that innate sensing of microbial infections will regulate adaptive immunity (*19, 20*). Thus, to understand B cell responses to viral infections, it is critical to investigate how surface Ag density and internal nucleic acids (iNA) of viruses impact Ab responses independently and collectively, both at early time points and over the long term. Dissecting the roles of virion surface Ag density and iNA on B cell response is especially relevant given the fact that Ag-specific B cells are sufficient to directly activate naïve $CD4^+$ T cells in response to virus-like particulate Ags without the involvement of dendritic cells (*21*).

Model Ags, such as the hapten 4-hydroxy-3-nitrophenyl (NP) acetyl and various polymers based on this hapten (*3*) have been indispensable to understand B cell responses to immunization (*22-26*). By contrast, model immunogens that facilitate the study of viral

features on B cell responses have significant limitations. Studies using live, attenuated or inactivated viruses have contributed substantially to our current understanding of B cell responses towards viruses (*6, 27-30*). However, it is difficult to isolate the roles of Ag valency and iNA due to the complex integrated supramolecular structures of viruses. For example, bacteriophage Qβ-derived virus-like particles (VLPs) are highly valuable tools that have offered significant mechanistic understanding in B cell responses to virus-like particulate Ags (*10, 14, 21, 31*). However, Qβ VLPs are mixtures of phage proteins and single-stranded RNA (ssRNA) self-assembled from *Escherichia coli* cell culture in diverse forms (*32*). Although these phage structural proteins are all foreign to mice or macaques, it has been challenging to assess the immunogenicity of these phage structural proteins in isolation due to the ability of phage coat proteins to bind ssRNA non-specifically. In fact, the ability to encapsidate foreign RNA is the basis on which the Qβ coat protein is used commercially for protection of heterologous RNAs (*33*). Attempts have been made to digest away RNA packaged inside VLPs to assess the immunogenicity of VLPs in the absence of nucleic acids (*31*). However, the VLPs after digestion still elicited IgG2a response in C57BL6/ mice (*31*), and the basis for this IgG2a has not yet been defined in TLR-7 gene knockout mice.

Moreover, Qβ is an icosahedral virus and it is known that the structural and mechanical features of icosahedral viruses are different from those of enveloped viruses (*34*), in terms of the spatial density of epitopes (*1*), rigidity and fluidity of the structures (*35*), which are all likely to influence immune responses (*36*). These differences between icosahedral and enveloped viruses confer cautions in extending mechanistic insights obtained from Qβ-based VLPs to enveloped viruses, such as SARS-CoV-2, influenza viruses and HIV-1.

Existing vaccine platforms such as ferritin nanoparticles (*37*) or computationally designed self-assembling protein nanomaterials (*38*) have been extensively studied and used in vaccine design and development (*39-41*). However, these structures lack iNA, which makes it difficult to assess the role of iNA in the context of virus-like Ags using these structures.

To overcome these limitations, we have developed a system of synthetic virus-like structures (SVLS) based on liposomes to mimic the structural features of enveloped viruses. These SVLS are constructed using highly purified biochemical ingredients and recapitulate the common biophysical features of naturally occurring enveloped viruses (*42-44*). Compared to bacteriophage Qβ-derived VLPs, the SVLS system herein uses lipid bilayers (*12, 45, 46*) instead of phage structural proteins to serve as the scaffold for the display of Ags, eliminating immune responses towards the scaffolds which may complicate data interpretation. The protein Ags of interest were then covalently conjugated onto the surface of these structures in an ordered array via site-specific maleimide chemistry, which allows a meaningful definition for the average spatial density of epitopes. To mimic naturally occurring viruses, we selected lipids that were abundant in natural plasma membranes to construct SVLS (Materials and Methods). We also avoided cationic lipids that are known to be immunostimulatory in nature (*36*), which were extensively used recently for the therapeutic delivery of nucleic acids in mRNA vaccines (*47*). More importantly, this system allows us to encapsulate iNA with *all-natural* phosphodiester backbone inside SVLS, which mimics the spatial confinement and chemical composition of a typical viral genome (*43, 44*).

To investigate the individual as well as the collective roles of surface Ag density and iNA on B cell Ab responses, it is highly desirable to independently modulate both surface Ag density and iNA on virion-sized Ags so that the resulting Ab response can be quantified in an animal

model. The system of SVLS allows us to do so due to the modular nature of these structures. Here, we first report the characterization of these SVLS structures bearing two different model Ags. We then describe the results of immunization using various SVLS structures in mice of two different genetic backgrounds: C57BL6 and BALB/c. We show that Ag display on virion-sized liposome serves as a standard alone danger signal to trigger rapid IgG secretion and seeds long-lasting production of IgG in the absence of TLR activation. Inclusion of iNA dramatically enhances the magnitude of IgG response in both the short and long-term so that a single injection of SVLS at very low Ag dose can lead to life-long Ab production in BALB/c mice. We show that Ag valency and iNA coordinate quantitatively to trigger durable antiviral IgG in a primary immune response such that iNA reduce the minimal epitope density and also CD19-dependence of SVLS responses. The resulting Ag-specific IgG's are characterized by ultralow off rates and offer potent neutralization even when elicited in a T-cell deficient background. These results reveal minimal structural determinants for several features of Ab responses observed previously in murine models of live viral infections, and emphasize the biophysical integrity of virus-like structures as the essential ingredient that gives rise to these features without any live infections.

Results

The characterization and the use of SVLS

We sought to generate reagents with highly purified components in order to model and modulate essential viral features in isolation and to co-ordinately define their impact on B cell responses. To do so, we prepared four sets of SVLS for the current study: two of them, schematically shown in Fig. 1A and B insets and termed pRBD and pHEL, respectively, are SVLS that display either purified receptor-binding domain (RBD) of the SARS-CoV-2, the causative agent of the COVID-19 pandemic (*48*); or a purified mutant version of hen egg lysozyme (HEL), a well-established model Ag for immunology studies. Each protein was displayed in a specific orientation at regulated densities on the surface of SVLS. The interior of pRBD and pHEL was filled with phosphate buffered saline (PBS). The other two sets: pRBD(iNA) and pHEL(iNA), schematically shown in Fig. 1C and D insets, are SVLS that not only display RBD or HEL on their surface, but also encapsulate nucleic acids inside these structures. All protein display was achieved through site-specific covalent conjugation on the lipid bilayer surface to ensure stability of the attachment with time (*42-44*). No proteins other than RBD or HEL were present in these structures. Fig. 1A through D show dynamic light scattering measurements of these structures, with diameters around 120 nm, which is very close to that of HIV, influenza virus and SARS-CoV-2 (*49-51*). Fig. 1E shows a representative epi-fluorescence image of individual pRBD(iNA) stained by a fluorescent RBD-specific Fab (Fig. S1). We determined the average number of antigenic molecules per structure, termed epitope density (ED) herein, using both ensemble and single-molecule fluorescence techniques that we established previously (*52-54*). As shown in Table S1, we

produced SVLS with a range of EDs for these structures that well covers the EDs observed for naturally occurring viruses (*1, 2*). As shown in Fig. 1F, the values of ED for pRBD(iNA) that we measured using the ensemble-based method overall agreed with ED values from the single-molecule fluorescence method (Fig. S1), with an adjusted R-square value of 0.997 from a linear regression analysis (the straight red line). The sensitivity of the single-molecule fluorescence method thus confirmed the SVLS with low ED values that we have prepared.

Most viruses infect their hosts through peripheral routes (*34*). To simulate a natural viral infection, we delivered a submicrogram dose of Ag into mice through subcutaneous injection of SVLS. This allows viral collection by the initial lymphatics to encounter B cells in the lymph nodes (*55*). A submicrogram dose of Ag is equivalent to picomoles of SVLS, which is a very low dose compared to those typically used for VLPs and also for conventional model immunogens in mice (*8, 9, 56, 57*). Natural viral infection does not involve any conventional adjuvants such as alum. Importantly, throughout, all the injections were performed without any exogenous adjuvants. As a result, the injections of SVLS only introduced the highly purified protein Ags and lipids for pRBD or pHEL, and additional encapsulated nucleic acids for pRBD(iNA) or pHEL(iNA).

Rapid IgG responses induced by SVLS without iNA

We found that a single injection of pRBD or pHEL at a submicrogram Ag dose and in the absence of iNA or any other adjuvants is sufficient to rapidly elicit Ag-specific IgG response in both C57BL/6 (B6) and BALB/c mice, provided that the ED on SVLS was above an apparent threshold. This is shown in Fig. 2A and 2B for various conditions that we tested

using pRBD and pHEL, respectively in B6 mice. For both SVLS, the Ag-specific IgG could be detected as early as day 5 (D5) post injection, 45±6 ng/ml anti-RBD IgG (Fig. 2A Condition 6 circle) and 51±15 ng/ml anti-HEL IgG (Fig. 2B Condition 6 circle), well above the detection limit of ELISA (Fig. S2). Because the reference monoclonal IgG's are affinity matured, the true concentrations of Ag-specific IgG's are likely to be even higher than these values, which reflect rapid extra-follicular responses by naïve B cells, with stronger responses on Day 11 (D11)(Fig. 2A-2B, Conditions 6 and 7 columns). The Ag-specific IgG responses were absent in several controls including PBS (Condition 1), soluble proteins (sRBD or sHEL, Condition 2), or an admixture of soluble proteins and control SVLS without conjugated proteins on the surface or iNA (Condition 3). Increasing the Ag dose of either sRBD or sHEL by tenfold also failed to elicit detectable Ag-specific IgG, consistent with the known requirement for adjuvants to produce immune responses to soluble proteins in mice. The exquisite sensitivity of animals towards pRBD or pHEL suggests that there are distinct signaling mechanisms involved in the sensing of these particulate Ags (*58*). In fact, *in vitro* studies using the same system of pHEL revealed that these SVLS were over 1000-fold more potent than respective soluble proteins in activation of Ag-specific B cells (*58*). Fig. 2A and Fig. 2B also revealed apparent thresholds of ED for IgG induction by either pRBD or pHEL in B6 mice. At the same Ag dose, an ED less than 25 was not sufficient to induce an Ag-specific IgG above background for either pRBD or pHEL (Fig. 2A-2B, Conditions 4 and 5). Stronger IgG responses were elicited with increasing ED for both pRBD and pHEL above the respective thresholds. Importantly, sera from mice immunized with pRBD (Conditions 6 and 7) could effectively neutralize HIV-1 pseudovirions (*59*) that displayed the cognate S protein of the SARS-CoV-2 *in vitro* (Fig. 2C), suggesting that the serum Abs induced by SVLS would be functional *in vivo* to offer the host some protection against infection of SARS-CoV-2. For both pRBD and pHEL, this rapid response induced IgG1, IgG2b and IgG3 in B6 mice

(Fig. 2D-I), but without IgG2c (Fig. S3). This distribution is consistent with what we observed previously for a self-Ag displayed on SVLS in B6 mice (*42*), where IgG2c is unique to immunization in the presence of nucleic acids. Also, it shows similarity to the subclasses of IgG induced in the context of live viral infections (*60*) yet distinct from those induced by the type II T-independent Ags (*61*). These results indicate that in the absence of iNA, a foreign protein displayed on the surface of a virion-sized liposome can trigger class-switch recombination (CSR) of the Ag-specific B cells *in vivo* to produce IgG1, IgG2b and IgG3, provided that the ED is above a threshold.

The presence of the HEL-specific IgG in B6 mice is intriguing because it is well established that the B6 strain is unresponsive to HEL due to its failure to generate a dominant MHC Class II determinant (*62*), which suggests that the initiation of the fast Ab response by these SVLS may be independent of T cell help. To test this formally, we immunized B6 mice that were deficient in both alpha/beta and gamma/delta T-cell receptors ($TCR^{-/-}$) (*63*) with either pRBD or pHEL. Statistical comparisons between Condition 7 (wild-type B6 or wtB6) and Condition 8 ($TCR^{-/-}$) for pRBD4 in Fig. 2A or between Condition 6 (wtB6) and Condition 8 ($TCR^{-/-}$) for pHEL3 in Fig. 2B for both D5 and D11 did not reveal significant differences (p-values>0.1 for all cases), suggesting that this IgG response was largely T-independent for both immunogens. Furthermore, Ab responses were also observed in B6 mice that were deficient in MyD88 ($MyD88^{-/-}$) (*64*) (Condition 9 in Fig. 2). Comparisons with respective wtB6 mice for both D5 and D11 did not reveal significant differences between Condition 7 (wtB6) and Condition 9 ($MyD88^{-/-}$) for pRBD4 in Fig. 2A or between Condition 6 (wtB6) and Condition 9 ($MyD88^{-/-}$) for pHEL3 in Fig. 2B (p-values>0.1 for all cases). These data ruled out the possibility that endotoxin or nucleic acid contamination of the SVLS produced these T-independent Ab responses, and suggest that the oriented display of surface epitopes

above a threshold ED on a virion-sized liposome can provide a sufficient '*danger*' signal to trigger a rapid class-switched Ab response that is detectable by ELISA, although the magnitude of this response is not very high. Consistent with these results, our studies using the same system of pHEL on MD4 B cells revealed that pHEL alone, without any additional adjuvants, can trigger robust MD4 B cell proliferation and survival *in vivo*, and can do so *in vitro* in the absence of MyD88, IRAK1/4 and CD40 ligation (*58*). Moreover, the Ab response induced by pRBD or pHEL was completely abrogated in B6 mice that were deficient in CD19 ($CD19^{-/-}$) (*65*) (Condition 10). CD19 is an important coreceptor on B cells (*66*) that lowers the threshold for BCR activation by complement-coated Ags (*67*, *68*) and is essential for B cell responses to membrane-bound ligands (*69*). These data indicate that CD19 is required for B cell production of IgG in response to a foreign protein displayed on the surface of a virion-sized liposome, even when the protein is displayed at a high density. Consistent with this, $CD19^{-/-}$ MD4 B cell proliferation in response to pHEL was also highly impaired *in vivo* (*58*).

Compared to wtB6 mice, BALB/c mice also mounted similar IgG responses on D5 after immunization with pRBD or pHEL (Fig. 2J circles). The IgG response included IgG1, IgG2b and IgG3, but without IgG2a (Fig. S4). The presence of these similarities with B6 suggests that the early Ab response is an immediate host response that is conserved in both strains of mice. However, the IgG response in BALB/c mice on D11 was much higher than those in wtB6 mice (Fig. 2J columns), due to a much stronger IgG1 response that dominated on D11 for both pRBD and pHEL (Fig. S4A and S4E), suggesting that there are major differences between the two mouse strains in the amplification of the Ab response beyond D5 after its initial activation.

Strong and rapid IgG responses induced by SVLS with various iNA

To examine the impact of iNA with natural phosphodiester backbones on the above IgG responses, we administered a single subcutaneous injection of pRBD(iNA) or pHEL(iNA) to mice at a submicrogram Ag dose without the use of additional adjuvants. We first measured the Ag-specific IgG responses in mice of B6 genetic backgrounds on both D5 (circles) and D11 (columns) post injection using ELISA, as shown in Fig. 3A and 3C for various conditions that we have tested for pRBD(iNA) and pHEL(iNA), respectively. These conditions included controls, SVLS of different ED, and SVLS containing different iNA sequences in either wtB6 or various gene knockout mice, as illustrated on the right in Fig. 3A and 3C. Many of these conditions induced strong Ag-specific IgG as early as D5 post injection. To quantify the amplification of the IgG response produced by iNA, we determined IgG titers for most conditions, as shown in Fig. 3B and 3D for pRBD(iNA) and pHEL(iNA), respectively. We observed a strong synergy between ED and iNA for SVLS encapsulating DNA1, a 20-mer single-stranded DNA that harbors two unmethylated CpG dinucleotides but has an all-natural phosphodiester backbone (Materials and Methods), as shown by Conditions 4 through 7 for both pRBD(DNA1) and pHEL(DNA1). When compared to either pRBD or pHEL without iNA, the titers of the IgG induced by these SVLS with DNA1 in wtB6 were all 10- to 1000-fold higher on D5 (circles, Fig. 3B and 3D), with even stronger responses on D11 (squares). As shown by several controls in Fig. 3A and 3C, the presence of iNA *internal* to SVLS was necessary for the strong and rapid responses observed, consistent with requirement for B-cell intrinsic TLR activation. Condition 1 is an admixture of soluble proteins with DNA1. Condition 2 and 3 are admixtures of DNA1 and

SVLS of different ED without iNA. Although unmethylated CpG DNA can activate TLR-9 (*70*), neither Condition 1 nor Condition 2 elicited Ag-specific IgG. Condition 3 elicited Ag-specific IgG but these responses were within error identical to those induced by SVLS alone without iNA (Fig. 2A and 2B), with p-values of 0.663 and 0.847 for pRBD3 on D5 and D11 and p-values of 0.728 and 0.787 on D5 and D11 for pHEL3 from one-way ANOVA tests. As we demonstrated previously (*43, 44*), when provided in a simple admixture, these nucleic acids of all-natural phosphodiester backbones were quickly degraded in biological milieu, consistent with the apparent lack of their effects in Conditions 1, 2 and 3. In contrast, when encapsulated within SVLS, the lipid bilayer structures protected iNA from nuclease degradation (*43, 44*), similar to those in enveloped viruses. As a consequence, these nucleic acids of all-natural phosphodiester backbones can unleash potent activity through intrinsic TLR activation after BCR mediated endocytosis of SVLS by the Ag-specific B cells *in vivo*.

Strikingly, we noticed that a very low ED of a few molecules of Ag per SVLS was sufficient to elicit these strong responses for both pRBD(DNA1) and pHEL(DNA1) (Fig. 3B and 3D, Condition 4). These results are surprising because an ED less than 25 was not sufficient to elicit an Ag-specific IgG above background for either pRBD or pHEL without iNA (Fig. 2). These data revealed several important conclusions that we can draw for mechanistic understanding of B cell responses to virus-like Ags. First, the threshold of ED observed for IgG elicitation by SVLS without iNA (Fig. 2) is not equivalent to the threshold of ED required for BCR-mediated Ag endocytosis. Second, the threshold of ED for BCR-mediated endocytosis is low, because just a few molecules of Ag per SVLS can mediate the potent effects of iNA in SVLS. Third, the higher value of ED threshold required for IgG elicitation by SVLS without iNA likely reflects the amount of BCR-mediated signaling that is necessary to drive CSR and IgG secretion in the absence of TLR activation. Fourth, the signal required

for CSR and IgG secretion in Ag-specific B cells can be achieved with ED alone, at the expense of a relatively high ED value (Conditions 6 and 7 in Fig. 2), or the collective signals from ED and intrinsic sensing of iNA together, which can work at a very low ED, thus demonstrating a quantitative coordination between Ag valency and innate nucleic acid sensing in the initiation of CSR and IgG secretion.

The synergy between ED and iNA described above was also observed for two other nucleic acids that were tested: DNA2 and RNA1 (Fig. 3B and 3D Condition 10 and 11). DNA2 is a 20-mer single-stranded DNA that harbors two unmethylated GpC dinucleotides but has all-natural phosphodiester backbone, which was usually used as a control for CpG-containing DNA. RNA1 is a 20-mer ssRNA that is highly conserved among SARS-CoV-1, SARS-CoV-2 and MERS-CoV, and encodes motif V of an essential RNA helicase in these coronaviruses (*71*) (Materials and Methods). Although the IgG response elicited by pRBD(DNA2) or pHEL(DNA2) was weaker than that of pRBD(DNA1) or pHEL(DNA1) at similar ED, DNA2 still enhanced IgG responses, indicating that the CpG dinucleotide motif was not required to observe this synergy. For pRBD(DNA2), the responses on both D5 and D11 were significantly higher than those induced by pRBD3, an SVLS of similar ED but without iNA (Fig. 2A Condition 6), with p-values of 0.0104 and 3.76e-4 from one-way ANOVA tests. For pHEL(DNA2), the responses on both D5 and D11 were also significantly higher than those induced by pHEL3, an SVLS of even higher ED but without iNA (Fig. 2B Condition 6), with p-values of 0.0494 and 0.0285 from one-way ANOVA tests. For pRBD(RNA1) (Fig. 3B Condition 11), although the IgG titer on D5 was lower than that induced by pRBD(DNA1)4, an SVLS of similar ED with DNA1 (Fig. 3B Condition 7, p-value=2.88e-8 from one-way ANOVA test), the IgG titer on D11 was statistically identical (p-value=0.356 from one-way ANOVA test). Therefore, CpG DNA is not unique in its strong potency for the synergistic

induction of Ag-specific IgG responses. A natural viral genomic sequence is sufficient to induce a strong and rapid IgG response that is comparable in its magnitude.

The use of B6 mice allows us to dissect genetic requirements for the robust Ab responses induced by SVLS containing iNA [SVLS(iNA) herein]. First, the IgG response was largely T-cell independent, as shown by the strong Ag-specific IgG observed in T-deficient mice for pRBD(DNA1) and pRBD(RNA1) (Fig. 3B, Condition 8 and 12), pHEL(DNA1) and pHEL(RNA1) (Fig. 3D, Condition 8 and 12). In contrast, the IgG induction required MyD88 or TLRs, as shown by the much attenuated IgG response in mice deficient in MyD88 for pRBD(DNA1) or pHEL(DNA1) (Fig. 3A and 3C, Condition 9); and in mice deficient in TLR-7 (*72*) for pRBD(RNA1) or pHEL(RNA1) (Fig. 3A and 3C, Condition 13). However, in mice deficient in CD19, strikingly, the presence of DNA1 internal to these SVLS can elicit a fast and strong IgG response as early as D5 for both pRBD(DNA1) and pHEL(DNA1) (Fig. 3B and 3D, Condition 14, circles). On D11, the IgG titer induced by pRBD(DNA1)4 in $CD19^{-/-}$ mice (Fig. 3B Condition 14) was as strong as that in wtB6 mice induced by the same agent at the same Ag dose (Fig. 3B Condition 7, p-value=0.356 from one-way ANOVA test). Likewise, the IgG titer induced by pHEL(DNA1)2 in $CD19^{-/-}$ mice on D11 (Fig. 3D Condition 14) was statistically identical to that in wtB6 mice induced by the same agent at the same Ag dose (Fig. 3D Condition 5, p-value=0.537 from one-way ANOVA test). These results are in sharp contrast to the requirement of CD19 by either pRBD or pHEL for induction of IgG in the absence of iNA (Fig. 2A-2B, Condition 10), and demonstrate the following: (1) a foreign protein on a virion-sized liposome alone requires CD19 to lower the signaling threshold needed for CSR and IgG secretion. (2) The presence of iNA helps bypass this requirement for CD19 due to the combined signals co-delivered by ED and intrinsic sensing of iNA to an Ag-specific B cell. (3) At the level of individual B cells (*73*) in

response to virus-like Ags *in vivo*, BCR and intrinsic TLR activation feed into a common pathway at or before the initiation of CSR and IgG secretion. As a result, deficiency in BCR-mediated signaling, either due to low ED (Condition 4, Fig. 3B and 3D) or the absence of coreceptor CD19 (Condition 14, Fig. 3B and 3D), can be compensated by the presence of iNA.

We next sought to compare the Ab responses induced by SVLS(iNA) to the commonly used bacteriophage Qβ VLPs platform (*10, 14, 21, 31*). The strong IgG induced by SVLS(iNA) was comparable in titers to those elicited by RBD or HEL conjugated on bacteriophage Qβ VLPs at the same Ag dose on both D5 and D11, despite the complete absence of the bacteriophage Qβ coat proteins in these SVLS(iNA). This was shown by Condition 15 in Fig. 3B for a Qβ-RBD conjugate with an ED of 200 and Condition 15 in Fig. 3D for a Qβ-HEL conjugate with an ED of 10 in wtB6. One-way ANOVA tests on these titer values revealed that Qβ-RBD induced the same level of RBD-specific IgG titers on D5 as pRBD(DNA1)1 and pRBD(DNA1)2, which were lower than those for pRBD(DNA1)3 and pRBD(DNA1)4; and Qβ-RBD induced the same level of RBD-specific IgG titers on D11 as pRBD(DNA1)3 and pRBD(DNA1)4, which were higher than those for pRBD(DNA1)1 and pRBD(DNA1)2 (Table S2A). For HEL, Qβ-HEL induced the same level of HEL-specific IgG titers on D5 and D11 as all pHEL(DNA1) (Table S2B). These results show that it is feasible to elicit IgG responses of a similar magnitude to bacteriophage VLPs using SVLS(iNA), despite the fact that the epitopes in these two platforms have very different two-dimensional mobilities.

Can these IgG molecules neutralize cognate viral infectivity? As shown in Fig. 3E (Conditions 4-7, 10-11, the same set of conditions as in Fig. 3A), the strong IgG induced by pRBD(iNA) as early as D5 after injection can potently neutralize HIV-1 pseudovirions that display the cognate S protein of SARS-CoV-2 *in vitro*, with an even stronger potency on D11 after immunization. These strong neutralizing activities were obtained for all iNA sequences that we tested, suggesting a broad relevance of these results to understanding virus-mediated B cell Ab responses. We noted that even in the absence of T cells, this neutralizing Ab (nAb) response was strong enough to potently neutralize cognate virions *in vitro* (Conditions 8 and 12 in Fig. 3E). These results are fully consistent with live viral infection literature showing potent nAb response in the absence of $CD4^+$ T cells (*60, 74-77*). Along a similar note, high-affinity nAb to SARS-CoV-2 can be made without T follicular helper cells in patients (*78*). Furthermore, this fast and potent nAb response was also mounted in $CD19^{-/-}$ mice (Condition 14 in Fig. 3E), demonstrating that the coreceptor CD19 can be bypassed for an immediate and yet potent nAb response.

Like we observed in the B6 background, strong and fast IgG responses were also induced by SVLS(iNA) in BALB/c mice as early as D5. As shown in Fig. 3F, BALB/c mice mounted strong IgG responses towards pRBD(DNA1) of varied ED (Fig. 3F left, Conditions 4-7) with comparable magnitudes to B6 on both D5 and D11. Likely due to the available T cell help in BALB/c mice for HEL, the IgG responses towards pHEL(DNA1) in BALB/c mice were even stronger on D11 than those in wtB6 (Fig. 3F right, Conditions 5-7), indicated by one-way ANOVA tests on these titer values (Table S3). Therefore, an IgG response was robustly triggered upon a single exposure to a submicrogram dose of Ag on SVLS(iNA) in the absence of any other adjuvants in both strains of mice. The similar magnitudes of these responses between B6 and BALB/c mice suggest that this rapid and strong IgG secretion in

response to the combined signals from ED and iNA in SVLS is conserved between the two strains and is highly efficacious against pseudovirions even in the absence of T cell help (Fig. 3E, Conditions 8 and 12). Moreover, for both RBD and HEL, these responses induced by SVLS(iNA) could be quantitatively compared to those induced by either Qβ-RBD (Fig. 3F left, Condition 15) or Qβ-HEL conjugate (Fig. 3F right, Condition 15) at the same Ag dose in BALB/c mice, confirming our results for this comparison in wtB6 mice. Collectively, these data reveal that live infection is not required to mount a fast and effective nAb response in mice. Instead, the two *danger* signals common to viral infection: ED and iNA in the context of a virus-sized structure are sufficient to trigger potent activation of Ag-specific B cells for CSR and IgG secretion. The integrity of this structure is important; leakage of iNA will compromise the efficacy of this process.

Both pRBD(iNA) and pHEL(iNA) induced IgG1, IgG2b, IgG2c and IgG3 in wtB6, with IgG2c being the dominant subclass for almost all the SVLS(iNA) (Fig. 4A through 4H). Analogous to wtB6, the IgG response in BALB/c induced IgG1, IgG2a, IgG2b, and IgG3, with IgG2a being the dominant subclass (Fig. S5) (*31*). All iNA, including DNA1, DNA2 and RNA1, induced IgG2c in B6 genetic background (Fig. 4C and 4G), which was in sharp contrast to the undetectable IgG2c upon pRBD or pHEL immunization without iNA (Fig. S3A and S3B). Therefore IgG2a/2c is uniquely induced via innate sensing of iNA (*31*), and SVLS(iNA) can induce all the IgG subclasses known in mice, in the absence of live infection or any other adjuvants. Furthermore, incorporation of iNA lowers the ED thresholds for each IgG subclass. With iNA, the level of IgG1 is now comparable between wtB6 and BALB/c particularly for pRBD(DNA1) on both D5 and D11 (Table S4 for one-way ANOVA tests). Moreover, the comparison between SVLS(iNA) and Qβ-conjugated Ags reveals that Qβ was a stronger inducer of IgG1 after D5 of immunization in both wtB6 (Fig. 4A and 4E,

Condition 15) and BALB/c mice (Fig. S5A and S5E, Condition 6). One possibility for this difference is the presence of multiple copies of the bacteriophage coat protein in Qβ VLPs, a foreign protein that is known to recruit T cell help in mice (*42*).

Duration of the IgG response induced by SVLS

How long will the Ag-specific IgG last in this primary immune response to SVLS at a submicrogram Ag dose without additional adjuvants? In live viral infections, the durability of the antibody response has been well documented (*30*) and, in humans, can range from 3 months to 75 years. We found that the Ag-specific IgG, in all cases, remains detectable over 300 days after a single injection of various SVLS, implying the generation of long-lived Ag-specific plasma cells (Fig. 5). As shown in Fig. 5A, the RBD-specific IgG in wtB6 mice elicited by pRBD(DNA1) peaked around 2 months after the exposure and then slowly decayed over time (blue symbols). Without internal DNA1 (triangles), the IgG response was at least 10-fold lower in magnitude, peaked around one month after exposure and then decayed. However, the level of RBD-specific IgG remained well above the detection limit of current ELISA (Fig. S2A), with the lowest concentration of RBD-specific IgG detected as 36±5 ng/ml for sera collected from wtB6 mice on D347 after a single immunization with pRBD3 (upper triangles). The diamonds represent the control sera from wtB6 mice immunized with an irrelevant Ag pHEL(DNA1)1. This control demonstrates that the IgG response is specific towards RBD but not to other components in SVLS such as lipids. As shown in Fig. 5B, both pRBD and pRBD(DNA1) induced long-lasting IgG whose concentrations in mouse sera increased with time in BALB/c mice, which is in sharp contrast to those in wtB6. The diamonds in Fig. 5B represent the control sera from BALB/c mice

immunized with the irrelevant Ag pHEL(DNA1)1, demonstrating the specificity of the IgG responses. The presence of DNA1 elicited much higher IgG concentrations, like those in wtB6 and consistent with the established view that innate sensing of nucleic acids controls adaptive immunity (*19*, *20*). As shown in Fig. 5C, sera collected from these immunized animals over this period neutralized more than 95% of pseudovirion infectivity, which included both wtB6 (grey symbols) and BALB/c mice (white symbols), even though the RBD-specific IgG in wtB6 waned over this period of time. Control sera from wtB6 immunized with pHEL(DNA1) showed no neutralization of virion infectivity (diamonds), demonstrating Ag specificity of the neutralizations observed. Continued monitoring of the BALB/c mice immunized with pRBD(DNA1) showed that these nAbs lasted over 600 days (Fig. S6, blue symbols), approaching the life span of these animals recorded in literature (*79*) and the sera remained highly effective in neutralization of cognate pseudovirions throughout (Fig. S6, white symbols).

Like RBD, qualitatively similar anti-HEL IgG responses were also observed in wtB6 (Fig. 5D) and BALB/c mice (Fig. 5E) upon a single injection of pHEL(DNA1) or pHEL. For all cases in wtB6, the levels of HEL-specific IgG rose initially, which was then followed by slow waning over time. Despite these decays with time, the concentrations of anti-HEL IgG in mouse sera remained well above the limit of detection by current ELISA (Fig. S2C). The diamonds in Fig. 5D represent the control sera from wtB6 mice immunized with an irrelevant Ag pRBD(DNA1)3, demonstrating that the IgG response is specific towards HEL but not to other components in SVLS such as lipids. It is worth noting that the peak concentrations for HEL-specific IgG induced by pHEL(DNA1) (blue symbols in Fig. 5D) were much lower than those for RBD-specific IgG induced by pRBD(DNA1) (blue symbols in Fig. 5A), likely due to the absence of T cell help for HEL in wtB6. As shown in Fig. 5E, both pHEL and

pHEL(DNA1) induced long-lasting HEL-specific IgG that increased with time in BALB/c mice, similar to those trends for pRBD and pRBD(DNA1) in BALB/c mice (Fig. 5B) but in sharp contrast to those in wtB6 (Fig. 5D). The diamonds in Fig. 5E represent the control sera from BALB/c mice immunized with the irrelevant Ag pRBD(DNA1)3, demonstrating the specificity of the IgG responses. Also, with internal DNA1, the concentrations of HEL-specific IgG (blue symbols in Fig. 5E) were much higher than those induced by pHEL without iNA (triangles in Fig. 5E), analogous to the situation in Fig. 5B for pRBD(DNA1) in comparison to pRBD in BALB/c mice over the same period of time. Therefore, a primary immune response induced by SVLS is long-lasting in both strains of mice. However, differences in genetic backgrounds contributed substantially to the quantitative evolution of the Ag-specific IgG concentrations with time. The presence of iNA induced a stronger and more durable IgG response compared to SVLS without iNA. Of note, the durable IgG response from pHEL(DNA1) in B6 mice (Fig. 5D blue symbols) suggests that long-lived plasma cells may have been generated in the absence of cognate T cell help (*80, 81*).

Affinity maturation of the IgG response induced by SVLS in BALB/c mice

The rising response of IgG with time in BALB/c mice suggests affinity maturation upon a single injection of a submicrogram dose of Ags in the absence of any other adjuvants. To characterize the affinity maturation of the IgG responses, we conducted Ag-specific binding measurements using BioLayer interferometry. First, the streptavidin sensor was coated with biotinylated Ag at a low density to ensure measurement of monovalent binding and dissociation by IgG, which was confirmed by comparing the rates of dissociation between a monoclonal mouse anti-RBD IgG and its Fab fragments (Fig. S7). Second, the sera from

individual animals at different times post injection were subjected to binding and dissociation measurements in real time, as shown in Fig. 6A and Fig. 6B for sera from a BALB/c mouse immunized with pRBD(DNA1)3 and in Fig. 6C and Fig. 6D for sera from a BALB/c mouse immunized with pHEL(DNA1)1, respectively. The amplitudes from real-time binding and dissociation allowed us to calculate the percentages of Ag-specific IgG that remained bound at the end of dissociation (Fig. S8A and S8B), which is a direct indicator of antibody affinity that is largely independent of their input concentrations (Fig. S8C). As shown in Fig. 6E, the percentages of Ag-specific IgG that remained bound at the end of dissociation showed a progressive increase until 2 months after the BALB/c mice were injected with either pRBD(DNA1) (red symbols) or pHEL(DNA1) (blue symbols), demonstrating affinity maturation. These quantitative trends were in sharp contrast to that for the sera from a B6 $TCR^{-/-}$ mouse that was injected with pHEL(DNA1)1 (green diamonds), which served as a negative control for affinity maturation. Moreover, it is surprising to note that for all cases, regardless of the specific Ags, the off rates of the Ag-specific IgG induced by either pRBD(DNA1) or pHEL(DNA1) were already at $(5.2\pm0.3)\times10^{-4}$ s^{-1} on D5, including the $TCR^{-/-}$ mouse (green diamonds in Fig. 6F). These values of off rates were comparable to the off rate of $(3.9\pm0.3)\times10^{-4}$ s^{-1} measured for the commercial monoclonal IgG2a for RBD (Fig. S7E), which is shown as a dashed line in Fig. 6F. This commercial IgG2a can potently block the binding of RBD to human ACE2 at a concentration of 0.05-0.25 µg/mL (BioLegend CAT#944803). Over the 6-month period after a single injection, the off rates of the Ag-specific IgG from all these animals underwent little or no changes (Fig. 6F). Thus, the affinity maturation for RBD-binding IgG Abs may be driven primarily by optimization of the on rate (*82, 83*).

To confirm this, we sought to verify the concentration of Ag-specific IgG in mouse sera using an approach that is orthogonal to ELISA. The accurate concentration will then allow us to determine the on rates without ambiguity. To this end, we first determined the concentration of Ag-specific IgG using a biotinylated Ag pulldown assay with streptavidin-coated magnetic beads (S-beads) followed by quantitative western blotting. These results were shown in Fig. 7A for the capture of RBD-specific IgG on D11 and D123, respectively, from a BALB/c mouse immunized with a single injection of pRBD(DNA1)3 in the absence of any other adjuvants. To confirm complete capture of the RBD-specific IgG, we used increasing concentrations of biotin-RBD, as indicated on Lanes 2, 3 and 4 for D11 sera and Lanes 6, 7, and 8 for D123 sera. Comparison with a standard curve (Fig. S9) obtained from the same western blots yielded the RBD-specific IgG concentrations for all these samples as shown in the bottom of Fig. 7A. For D11 sera, Lanes 2, 3 and 4 yielded very similar concentrations, with an average of 0.139±0.007 mg/mL. A one-way ANOVA test among Lanes 2, 3, and 4 returned a p-value of 0.717; therefore, there were no statistically significant differences among these measurements with increasing biotin-RBD, which indicates that we captured nearly all RBD-specific IgG from D11 sera. Also, this concentration was much higher than that measured by ELISA (Fig. 5B), suggesting that the standard curve obtained from affinity-matured mAb1 significantly underestimates the concentration of anti-RBD IgG on D11. For D123 sera, Lanes 6, 7 and 8 also yielded very similar concentrations, with an average of 0.356±0.007 mg/mL. A one-way ANOVA test among these lanes returned a p-value of 0.96, again demonstrating no statistically significant differences among these measurements with increasing biotin-RBD and indicating that we have captured nearly all RBD-specific IgG from D123 sera. However, a one-way ANOVA test between D11 and D123 measurements returned a p-value of 2.9e-5, indicating that the concentrations of RBD-specific IgG were significantly different in the sera from these two different dates. These concentrations

allowed us to measure the on rates of RBD-specific IgG to RBD using BioLayer interferometry by using serial dilutions of the respective sera, as shown in Fig. 7B for the series of binding curves from D11 sera and Fig. 7C for the series of binding curves from D123 sera (note the different scales of the y-axes in Fig. 7B versus 7C). All these binding curves can be well described by exponential functions (solid black lines). We plotted the observed rate constants from these exponential fits as a function of the RBD-specific IgG molar concentration in Fig. 7D, which showed expected linear dependence for both D11 and D123 sera (straight red lines). The slopes of these lines determined the bi-molecular rate constants for the binding between RBD and RBD-specific IgG, which were $(4.2\pm0.2)\times10^4$ $M^{-1}s^{-1}$ on D11 and $(1.2\pm0.1)\times10^5$ $M^{-1}s^{-1}$ on D123. Therefore, the binding rate constants increased almost 3-fold as a result of affinity maturation over the period from D11 to D123.

Discussion

Two biophysical attributes shared by most animal viruses are the surface display of virus-specific proteins at certain densities and the encapsulation of viral nucleic acid genomes inside the virion. It has been well documented that Ag valency has profound effects on B cell response and differentiation *in vivo* (*4*). It is also established that innate sensing of microbial NA can control and regulate adaptive immunity (*19, 20*). However, in the context of a virus-like particulate Ag, how epitope valency and innate NA sensing coordinate with each other to shape B cell Ab responses has been less clear. Using a unique system of SVLS that enables us to independently vary highly pure viral features, here we have characterized the individual as well as the collective effects of ED (i.e., antigen valency) and iNA on both immediate and

long-lived B cell Ab responses. This study has uncovered several new mechanistic aspects of B cell responses to virus-like particulate Ags.

(1) CSR induced by virus-like Ag *in vivo* independently of T cells or TLR activation.

Although the molecular mechanisms of CSR have been well studied (*84, 85*), the antigenic signals that induce CSR *in vivo* remain incompletely understood (*86*) and a subject of active study (*87, 88*). Studies of humoral immunity upon viral infection have revealed that for the majority of viruses, nAbs are induced rapidly, within just a few days after infection (*29*). These early antibodies are isotype class-switched independently of $CD4^+$ T cells (*60, 74-77*), and are potent in viral neutralization (*60, 74, 76, 77*). However, the mechanisms responsible for these class-switched nAb responses have been less clear. It was concluded that factors induced during live virus infection appeared to be required to induce the CSR (*28*). In a recent study, it was shown that bacteriophage Qβ VLPs could induce class-switched and somatically mutated memory B cells in the absence of T cell help and also Bcl-6 expression in pre-germinal center B cells (*89*). However, because Qβ VLPs possess both high ED and ssRNA packaged inside the particles, which could serve as a potent TLR-7 ligand, it remains unclear if ED alone could trigger CSR in the absence of T cells *in vivo*. Here using SVLS, we showed that class-switched Ab responses can be induced by a foreign protein displayed on the surface of a virion-sized liposome in the absence of T cells or TLR engagement, provided that the ED is above a threshold. This is true for both RBD and HEL, two unrelated Ags, suggesting that this may be a general phenomenon for B cell responses to Ags displayed on virus-sized structures. In fact, these results are also consistent with what we reported previously, where a liposomal display of a self-Ag can induce a class-switched IgG response (*42*), although the Ag dose for the self-Ag was much higher than the Ag dose for the two

foreign proteins in the current study. In the absence of iNA, the oriented display of proteins above a threshold ED on a virion-sized liposome can induce IgG1, IgG2b and IgG3 in both wtB6 and BALB/c mice, true for both foreign Ags in this study and also the self Ag that we studied previously (*42*). Thus, neither live infection nor any other adjuvants are necessary to initiate this class switching. Together, these results demonstrate that the oriented display of viral surface proteins above a threshold ED on a virion-sized sphere is sufficient to serve as a stand-alone '*danger*' signal to trigger CSR and an IgG response in the absence of T cells or Toll-like receptor signaling. Consistent with this view and as we just showed recently, Ag-specific B cells use a signaling mechanism that is distinct from that for soluble Ags to sense these structures, notably through evasion of Lyn-dependent inhibitory pathways to initiate proliferation (*58*). Furthermore, these structures without iNA could maximally activate the NF-κB signaling pathway in Ag-specific B cells in a manner that mimics T cell help independently of MyD88, IRAK1/4 and CD40 ligation (*58*). We hypothesize that the NF-κB signaling triggered by ED in the absence of iNA can drive the expression of activation-induced cytidine deaminase, which then initiates CSR *in vivo*. Alternatively, cytokine production *in vivo* by B cells or other immune cells may contribute. These possibilities remain to be tested.

In the context of viral infection, this immediate CSR and IgG secretion, even in the absence of affinity maturation, could offer numerous benefits to the host. Unlike IgM, the smaller size of IgG allows easy access to extravascular space and offers protection at those sites (*87*). Class-switched B cells also have an advantage in signaling and survival over unswitched B cells due to the difference in the Ig cytoplasmic tail (*90*). Besides its role in direct neutralization of virion infectivity, the IgG can hexamerize through its Fc after Ag binding, which leads to potent activation of the complement cascade (*91*). It has been known for a

long time that natural killer (NK) cells can bind to immune-complexed IgG via CD16-FcγRIIIA and this interaction activates the lytic mechanism of NK cells and also induces the production of lymphokines (*92*, *93*). Thus, the secretion of IgG, even a germline version, can produce multiple levels of effector functions for antiviral defense.

(2) Potency of the T-independent IgG.

Another surprising result from the current study is that these rapidly produced Ag-specific IgG elicited by SVLS exhibit very slow off rates that are less than 0.001 s^{-1}, which are comparable to that of a commercial mAb (Fig. 6F). These IgGs emerged as early as Day 5 post Ag exposure, regardless of the specific protein Ag or the mice strains and even in the absence of functional T cells (Fig. 6F), suggesting that this may be a general phenomenon in mice. The IgG from both B6 and BALB/c mice can potently neutralize cognate pseudovirions (Fig. 5C). These data are very much consistent with previous studies of live infection by vesicular stomatitis virus (VSV) and influenza virus in murine models. It has been found that VSV-specific IgG in germline configuration is already highly protective against VSV infection (*94*), which does not require somatic hypermutation or affinity maturation (*94*). Similar results also occur in murine models of influenza virus infection (*95*). The current study offers a mechanistic explanation for these live infection data: (1) live infection produced virions; (2) the integrative virion structure, i.e., the ordered display of a foreign Ag on the surface of a virion-sized structure, together with iNA, can robustly activate naïve Ag-specific B cells to initiate CSR and secrete IgG that is independent of viral replication or any other adjuvants; and (3) the IgG has an intrinsically slow off rate that can offer effective neutralization of cognate virions.

An optimal, highly potent IgG should have both a fast on rate and a very slow off rate so that it can bind its target with high affinity. Despite a very slow off rate, this early version of RBD-specific IgG is not optimal because of a slow on rate. As shown in Fig. 7D, the RBD-specific IgG on D11 post injection has an on rate of $(4.2\pm0.2)\times10^4$ $M^{-1}s^{-1}$, which is more than tenfold slower than the on rate of the commercial RBD-specific mAb1 that we have measured, $(6.1\pm0.3)\times10^5$ $M^{-1}s^{-1}$ (data not shown). However, we hypothesize that this immediate IgG response is at evolutionary advantage to the host because defects in IgG on rate can be potentially compensated for by a high concentration of the IgG rapidly secreted in the context of an extra-follicular response to acute viral infection, which is triggered by the combined signals from ED and iNA presented by intact virion structures. This suggests that upon germinal center formation in a suitable host, the major improvements conferred by affinity maturation to these IgGs are likely in the on rates of Ag binding. In fact, this is the case in our data (Fig. 7D): over a period of 2 months (Fig. 6E), the on rate of the RBD-specific IgG increased by roughly 3-fold from the single injection. Also, in murine models of live infection by VSV, it was discovered that the efficiency of neutralization is highly correlated with the on-rate of IgG that arises as a result of live viral infection (*83, 96*), suggesting that this optimization of IgG on-rate is indeed the case for live viral infections. In a separate study, enhancement of IgG on-rate during affinity maturation was also suggested by human nAbs directed towards infection by the respiratory syncytial virus (*82*). Therefore, in both mice and humans, live infections of two different viruses optimized the on-rate of IgG, suggesting that the germline version of IgG has excellent off rates to provide effective protection. Taken together, this is a highly effective strategy for antiviral defense. The speed together with the magnitude of this response is largely independent of T cells, affording the host with a mechanism of fast and strong nAb response that would be critical during the early onset of an antiviral defense. It's important to note that, in addition to binding rates, an IgG's

potency for neutralizing viral infectivity is also influenced by the virus' ED. Specifically, the ED of the virus can impact the stability and effectiveness of bivalent binding by the IgG, which is more effective than monovalent binding (*2, 97*).

(3) The quantitative coordination between ED and iNA to initiate IgG responses.

The synergy between a protein Ag and a TLR agonist in a B cell Ab response has been well recognized in literature (*14, 16-18, 98, 99*). However, we are still intrigued by our data showing that iNA can compensate for the deficit in ED/BCR-mediated signaling to allow for the potent induction of CSR and IgG secretion. These results in both wtB6 and CD19$^{-/-}$ mice have several implications regarding the initial events in Ag-specific B cell activation. First, BCR-mediated endocytosis can occur with as low as a few molecules of Ag per virion-sized structure *in vivo*. However, this low ED alone, is insufficient to trigger CSR and IgG secretion, which requires a much higher threshold of ED, as schematically shown in Fig. 8. This result pertains to both basic B cell biology and also B cell antiviral responses. Studies have attempted to resolve the minimum BCR signaling threshold required to internalize Ags *in vivo* (*100*). One study has suggested the presence of such a threshold in the avidity of BCR-Ag interactions (*16*). However, this question is not resolved due to the intrinsic complexity in B cell biology. Hou et al. reported that BCR signaling and internalization are mutually exclusive events, i.e., each BCR can undergo only one of two events, signaling or internalization, but not both (*101*). This suggests that the threshold for BCR-mediated internalization may not be equivalent to the threshold for BCR signaling. Consistent with this view, our results here clearly showed that *in vivo*, the threshold of ED required for BCR-mediated internalization is much lower than the threshold of ED alone required for CSR and IgG secretion.

Second, the capability of iNA to compensate for the deficiency of ED to mediate CSR and IgG secretion indicates that at a single-cell level, ED and iNA-mediated signaling converge to a common pathway that eventually leads to CSR and IgG secretion (Fig. 8). This quantitative coordination between Ag valency and iNA has several implications for our understanding of B cell responses to virus-like particulate Ags. Naturally occurring virions have densities of surface proteins that vary over several orders of magnitude, ranging from 200 to 30,000 molecules per μm^2 (*1, 2*) and yet little is known about how this varied spatial density of viral surface Ags contributes to the immunogenicity of viruses. The capability of mouse B cells to respond to virus-like Ags with as few as several molecules of surface Ag indicates that they can respond to a broad spectrum of viruses regardless of the densities of viral surface Ags, provided that there are potent TLR-activating iNA sequences inside these virions that are also accessible for TLR activation. On the other hand, because this mechanism is so potent in nAb induction, viruses that are known to co-evolve with their hosts may evolve to optimize their genome sequences to minimize potent TLR-activating iNA sequences such as CpG dinucleotides, or to encode virulence factors to antagonize this mechanism. In fact, it has been found that CpG dinucleotide sequences are suppressed in the genomes of virtually all eukaryotic viruses with a genome size < 30 kb (*102*), including that of HIV-1 (*103*). Moreover, viruses may evolve to control the accessibility of their genomes for recognition by TLRs, given the fact that ligand availability for TLR activation is finely regulated *in vivo* to balance outcomes in antiviral responses and autoimmunity (*104*). One major difference between SVLS and natural viruses is the accessibility of iNA. In SVLS, the iNA is accessible for recognition by TLRs upon BCR-mediated endocytosis. In natural viruses, many viral genomes are packaged with viral structural proteins. One strategy that viruses can evolve is to preclude the access of viral genomes by TLRs until the virion is ready to uncoat

its genome to start its life cycle of replication. Given the huge differences in the levels of Ag-specific IgG with and without iNA, the modulation of TLR activation may naturally give rise to distinct levels of antibody responses. Whether this mechanism works in naturally occurring viruses remains to be tested. Table S5 summarizes the mechanisms of IgG responses from current studies together with their implications for the understanding of viral immunogenicity in mice. On a similar note, recently work by the Casali group also showed that BCR-TLR co-engagement can induce CSR and hypermutated nAb response in the absence of T cells (*105*).

(4) Role of CD19 in B cell response towards virus-like Ags.

CD19 is an important coreceptor for B cell Ag receptor activation (*66, 67, 69*). It lowers the threshold of signaling for BCR activation by complement-coated Ag (*67*), essential for B cell activation in response to membrane-bound Ags *in vitro* (*69*) and crucial for B cell response to T-cell-dependent Ags *in vivo* (*66*). However, the role of CD19 in B cell sensing and response to virus-like Ags has not been established. Here we show that CD19 is required for B cell responses to SVLS *in vivo* in the absence of innate NA sensing but can be bypassed with intrinsic TLR activation. Consistent with these results, our adoptive transfer studies using purified MD4 follicular B cells showed the requirement of CD19 for responses to pHEL *in vivo* (*58*). At a mechanistic level, these results imply that CD19 helps amplify ED/BCR-mediated signaling, which is required for CSR and IgG secretion in the absence of TLR activation. However, in the presence of strong TLR activation, this CD19-mediated amplification of BCR signaling becomes redundant and thus dispensable. In particular, our finding that SVLS(iNA) can induce potent IgG response without CD19 (Fig. 3) may be useful for patients who suffer from antibody-deficiency syndrome due to mutations in the

CD19 gene (*106*). These patients responded poorly to vaccines such as rabies (*106*). In this case, an alternative vaccine formulation strategy to include potent TLR-activation iNA in SVLS may be useful for a better Ab response.

(5) Durable IgG from a primary response to SVLS.

VLPs are known to induce long-term humoral immunity in mice although the mechanisms behind this phenomenon are less well understood (*9*). Our current study has exclusively focused on the primary Ab responses to SVLS at a very low Ag dose. At present, the relationship between short-term expansion of plasmablasts and generation of long-lived plasma cells for durable protection is being actively studied (*27, 107*). It is thus notable that all the IgG responses to SVLS are long-lived (Fig. 5). SVLS not only initiated rapid IgG responses, but also seeded the production of IgG in the long-term, consistent with the literature that long-lived plasma cells form early in an immune response for both T-independent and T-dependent Ags (*80, 108*). The secretion of IgG in response to SVLS(iNA) is life-long in BALB/c mice (Fig. S6). These results indicate that ED above a threshold on a virus-sized structure, in the absence of any other adjuvants or TLR activation, can induce the production of long-lived plasma cells. The presence of iNA can substantially enhance the magnitude of the IgG response for both the short and long-term, although it doesn't alter the up or down trends of the IgG response in the long-term. Overall, these results are consistent with the literature that Ag valency is important for a durable Ag response (*109, 110*), and that innate sensing of microbial infection through TLRs will control and regulate adaptive immunity (*19, 20*).

However, the differences between mouse strains in the long-term trends of IgG in response to the same immunogens at the same Ag dose are very intriguing. Within the same strain, regardless of the specific Ags or the inclusion of iNA, the evolution of IgG with time followed the same up or down trends (Fig. 5). Therefore, the differences in long-term Ab response appear to be more related to strain differences instead of the specific Ags or TLR signaling. Along this line of strain differences, we noted that BALB/c mice mounted much stronger IgG1 than wtB6 on D11 for both pRBD and pHEL (Fig. S4A and S4E), even though the levels of Ag-specific IgG were overall comparable on D5 between the two strains (Fig. 2J). These results suggest that early on in an immune response towards virus-like Ags (between D5 and D11), BALB/c mice amplify the activation signals conveyed by ED more than wtB6. Whether this difference observed on D11 may lead to differences in IgG long-term trends between the two strains remains to be studied. Moreover, what causes these differences between wtB6 and BALB/c towards the same multivalent SVLS Ag, and whether these differences are imparted from the original Ag exposure (*110*) (differences in precursor frequency for example) or due to differences that occur at a later stage after the initial B cell activation and MHC class II Ag presentation (*111*) remain to be tested.

(6) SVLS as new model Ag for dissection of B cell antiviral response and potential vaccine platform.

In comparison to the complex bacteriophage VLPs that have been used as a model Ag for understanding of B cell responses to virus-like particulate Ags, SVLS use the minimal essential viral components to model virus-like Ags, yet the potency of the IgG response triggered by these SVLS can be compared to that of well-established bacteriophage VLPs, suggesting that this model Ag has captured the key ingredients in VLPs for B cell response.

The three biochemical ingredients in SVLS(iNA) are commonly found in naturally occurring enveloped viruses: a foreign protein, iNA and neutral lipids. This platform is highly modular and can be readily adapted to different proteins. We have tested RBD, HEL as shown in the current study and a self-Ag peptide previously (*42*). Therefore, this platform has the potential for use in other viral protein systems for understanding of B cell Ab response in the absence of an active infection. The modular nature of the SVLS structure is particularly desirable for dissecting the roles of individual components in B-cell antibody responses towards complex immunogens such as virions, and may be useful for studying mucosal immunity against virus-like Ags, which is important for protection from several human viral pathogens (*112*). The completely synthetic nature of these SVLS could also be useful for vaccine design and formulation from several different perspectives. First, the ability to use iNA for intrinsic TLR activation can dramatically enhance B cell activation, which may be especially desired for activating those very rare Ag-specific B cells. In this regard, SVLS may be at advantage compared to ferritin nanoparticles (*37*) or computationally designed self-assembling protein nanomaterials (*38*). Second, SVLS uses a stable formulation (*43, 44*) to preserve the integrity of virus-like structures for presentation of protein antigens in their native conformations without any associated viral infectivity, which may be at advantage compared to the platform of inactivated viruses, where formaldehyde and/or detergent treatment can alter conformations of protein antigens or even destroy the structures of viruses that are critical for B cell activation (*110*). Third, the regulatory requirements for purified synthetic agents could be less complex compared to products directly derived from cell culture (*113*), and last, the use of nucleic acids with native phosphodiester backbones in SVLS without the need for nuclease-resistant phosphorothioate could substantially reduce the cost of vaccine manufacture.

MATERIALS AND METHODS

Synthesis of SVLS

All SVLS used throughout this study were prepared following protocols we published previously (*42-44*). These SVLS were constructed using nonimmunogenic lipids, with phosphatidylcholine and cholesterol comprising ≥ 99% of all lipids. These structures display protein antigens (Ags) of choice in a specific orientation on their surfaces with a regulated ED that quantitatively mimics the surface of naturally occurring viruses (*1, 2*) (Fig. 1). The HEL recombinant protein used in this study contains two site-directed mutations at R73E and D101R and was overexpressed in *E. coli* and purified to >95% purity following our established protocols (*43*). The SARS-CoV-2 RBD recombinant protein used in this study was overexpressed using 293F cells and also purified to >95% purity following our established protocols (*44*). DNA1, DNA2 and RNA1 were custom synthesized by IDT. The sequence of DNA1 is as follows, 5'-TCCATGACGTTCCTGACGTT-3'. The sequence of DNA2 is as follows, 5'-TCCATGAGCTTCCTGAGCTT-3'. The sequence of RNA1 is as follows, 5'-ACUGUUGAUUCAUCACAGGG-3'. Epitope density (ED) was quantified using methods that we established previously (*42-44, 52*) that were also validated by single-molecule fluorescence techniques (Fig. S1) that were developed and established in house (*53, 54*). For SVLS with iNA, the average number of internal nucleic acids (iNA) molecules per SVLS was also quantified using methods that we established previously (*43, 44*). Control SVLS had no surface protein conjugation nor internal encapsulated agents.

Conjugation of RBD or HEL to bacteriophage Qβ virus-like particles (VLPs)

The bacteriophage Qβ VLPs were prepared as described (*114*). The purified RBD or HEL recombinant proteins, which each contained a single reactive cysteine near their respective C-termini, were conjugated to the surface of the VLPs using the heterobifunctional crosslinker Succinimidyl-6-[(β-maleimidopropionamido)hexanoate] (SMPH). Briefly, the VLPs were first derivatized with SMPH at a 10-fold molar excess of SMPH over Qβ coat protein. The mixture was incubated at 22°C for two hours and the excess crosslinker was removed by centrifugation at 4°C in an Amicon Ultra-4 centrifugal unit with a 100 kD cutoff. The RBD or HEL protein was then added to the derivatized VLPs and the mixture was incubated at 4°C overnight for RBD or at 20°C for 1 hour for HEL. Free proteins were then removed by centrifugation at 4°C in an Amicon Ultra-4 centrifugal unit with a 100 kD cutoff. The quantity of conjugated proteins was assessed using a denaturing polyacrylamide gel based on the intensity from silver staining in comparison with a standard curve obtained from the same gel.

Mice immunizations

All animal procedures were approved by the University of Michigan Animal Care and Use Committee. Female C57BL/6 or BALBc/J mice (8 weeks, Jackson Laboratory) were used for immunizations. Prior to inoculation, all injection samples were filtered through a 0.45 µm pore size membrane to eliminate potential microbial contamination. 100 µL samples at a dose between 0.1 and 0.48 µg of respective protein Ags were injected into each mouse subcutaneously, 50 µL in each flank. Throughout the entire study, no adjuvants other than the SVLS were administered unless otherwise noted and only a single injection was administered throughout. Mouse blood was collected submentally using Microvette serum collection tubes (Sarstedt) three days before the first injection, and 5 days thereafter

following specified blood collection schedules. The sera were harvested by centrifugation at 10,000 g for 5 minutes, aliquoted and immediately frozen and stored at -80°C.

Four strains of gene knockout mice were purchased from Jackson Laboratory: $Tcrb^{tm1Mom}$/ $Tcrd^{tm1Mom}$ (#002122) ($TCR^{-/-}$ herein) was deficient in both alpha beta and gamma delta T-cell receptors (*63*). $Myd88^{tm1.Defr}$ (#009088) ($MyD88^{-/-}$ herein) encodes a deletion of exon 3 of the myeloid differentiation primary response gene 88 (*64*). $Cd19^{tm1(Cre)Cgn}$ (#006785) ($CD19^{-/-}$ herein) has a Cre recombinase gene inserted into the first exon of the CD19 gene thus abolishing CD19 gene function (*65*). $Tlr7^{tm1Flv}$ (#008380) ($TLR7^{-/-}$ herein) has a segment of exon 3 of the Toll-like receptor 7 gene replaced by a lacZ gene and a loxP-flanked neomycin resistance cassette thus abolishing the function of Toll-like receptor 7 (*72*). Gene knockout mice were housed in a germ-free environment and immunization protocols were carried out as described above.

Enzyme-Linked Immunosorbent Assay (ELISA)

Blood serum was tested by ELISA in order to quantitate Ag-specific IgG responses to various immunizations. 96-well plates (Nunc MaxiSorp, Invitrogen) were coated overnight at 4°C with either 200 ng of sHEL or 320 ng of sRBD per well in PBS. After blocking with 1% Bovine Serum Albumin (BSA, Fisher) in PBS, mouse sera of specified dilution factors were added to each well for incubation at 22°C for 2 hours. After three washes using PBS with 0.05% Tween 20, secondary goat anti-mouse IgG Fc-HRP antibody (# 1033-05, Southern Biotech) was added in blocking buffer at 1:6000 dilution and incubated for 1 hour at 22°C. Following three washes, 100 µL of substrate 3,3',5,5'-Tetramethylbenzidine (Thermo Scientific) was added to each well and incubated in the dark for 10 minutes. The reaction

was stopped by addition of 100 µL 2M sulfuric acid in each well. The optical density of each well at 450nm was measured using a microplate reader (Bio-Tek Synergy HT). All the OD values reported were background subtracted by comparison between two wells that were coated with soluble protein and PBS, respectively. To estimate Ag-specific IgG concentration in mouse sera based on ELISA standard curves (Fig. S2), all sera samples were properly diluted to reach final OD values between 0.2 and 0.5 before interpolation.

To determine the titers of Ag-specific IgG, we used a serial dilution of serum (from 1:100 dilution to 1:10,000,000 by a dilution factor of 10) for ELISA with the sHEL or sRBD protein. Cutoff values were calculated using the following equation as reported (*115*): Cutoff = $\bar{X} + SD \cdot f$, where X□ and SD are the mean and standard deviation of control well OD reading values, f is the standard deviation multiplier corresponding to different confidence levels. Specifically in our assays, f = 2.631 when the number of control wells was 4 and the confidence level was 95%. The titer value was determined as the highest dilution factor of the serum that still yielded an OD450 value higher than the above cutoff value in ELISA.

To determine the subclasses of IgG antibodies elicited in mice upon immunization by various agents, we used the following secondary antibodies during ELISA: goat anti-mouse IgG1 HRP antibody (#1071-05, SouthernBiotech), goat anti-mouse IgG2a HRP antibody (#1081-05, SouthernBiotech), goat anti-mouse IgG2b HRP antibody (#1091-05, SouthernBiotech), goat anti-mouse IgG2c HRP antibody (#1078-05, SouthernBiotech), and goat anti-mouse IgG3 HRP antibody (#1101-05, SouthernBiotech).

Preparation of HIV-1 virions pseudotyped with SARS-CoV-2 envelope

The HIV-1 pseudotyped with SARS-CoV-2 envelope was prepared following the published protocols (*116*) but with modifications. Briefly, HEK 293T/17 cells (ATCC, Manassas, VA) were cultured at 37°C with 5% CO_2 in DMEM supplemented with 10% FBS (HyClone Laboratories, Logan, UT). 10^6 293T cells in a 2-mL culture volume were seeded overnight in a 35-mm dish before transfection using the TransIT LT-1 transfection reagent (Mirus Bio, Madison, WI). For each dish, 2 μg of the provirus-containing plasmid pNL4-3 luc R^-E^- (*117*) (ARP-3418, NIH AIDS Research and Reference Reagent Program) was used to make the transfection reagent mixture, together with 1 μg of envelope expression plasmid pcDNA3.1 SARS-CoV-2 S D614G (*116*). The plasmid pcDNA3.1 SARS-CoV-2 S D614G was a gift from Jeremy Luban (Addgene plasmid # 158075; http://n2t.net/addgene:158075; RRID:Addgene_158075). The RBD amino acid sequence 328-537 encoded in this plasmid is identical to the sequence of RBD that we studied here. The transfection reagent mixture was incubated at room temperature for 15 min before drop wise addition to the culture medium, as we did previously (*118*). At 6 hours post transfection, the culture medium together with the transfection reagents was replaced with fresh complete medium and the incubation was continued at 37°C with 5% CO_2. At 48 hours post transfection, the entire culture medium containing single-cycle HIV-1 viruses was collected and filtered through a 0.45-μm syringe filter (Millex-HV PVDF, Millipore). The filtrate was then aliquoted on ice, flash-frozen in liquid nitrogen and stored in a -80°C freezer. The concentration of virion particles was quantitated using a HIV-1 p24 ELISA kit (CAT#XB-1000, XpressBio) as we described previously (*118*).

Virion neutralization assay

The virion neutralization assay follows the protocols we established previously but with important modifications (*118*). HIV-1 virions pseudotyped with SARS-CoV-2 envelope containing 9 ng of HIV-1 p24 were incubated with various mouse sera at 37°C for one hour, and then diluted with complete medium by 8-fold in volume for the sera to initiate infection of Huh-7.5 cells at 37°C for 2 hours. At the end of 2 hours, fresh medium was added to each well in a 24-well plate and the incubation was continued at 37°C with 5% CO_2. Luciferase activity was measured 48 hours after infection. Briefly, the culture medium was removed and replaced with 100 μL of complete medium. 100 μL of Bright-Glo™ reagent (CAT#E2610, Promega) that was just warmed to room temperature was then added to each well. The cells were incubated for three minutes at room temperature to allow cell lysis. After three minutes, 100 μL of lysate from each well was transferred to a single well in a 96-well black microtiter plate (Costar). Luminescence was measured using a Synergy™ HT multi-mode plate reader (BioTek Instruments Inc., Vermont) and background luminescence was subtracted using Huh-7.5 cells without virus infection. For comparison among different immunization groups in Fig. 2C and Fig. 3E, the luminescence readings for cells incubated with sera from PBS-injected mice was set as 100%. The luminescence readings from other groups were all normalized based on this and plotted as a percentage of remaining infectivity. For comparison among different time points post immunization, the luminescence readings for cells incubated with sera from each group of mice before injections was set as 100%. The luminescence readings from other time points for the same group were all normalized based on this and plotted as a percentage of remaining infectivity.

BioLayer interferometry measurements

Affinity maturation of Ag-specific antibodies in animal sera together with binding and dissociation rate constants were measured using BioLayer interferometry. Briefly, the streptavidin sensor (Sartorius Corp) was coated with 50 nM RBD or HEL in 1×PBS for 30 min at 20°C, which was followed by washing in PBS for 10 min. For this application, both RBD and HEL were site-specifically biotinylated in house using EZ-link maleimide-PEG2-biotin (ThermoFisher, CAT#A39261). After sensor loading, they were dipped into antibodies or sera of varied dilutions in Buffer 1 to measure the binding in real time using an OctetRed BioLayer Interferometer equipped with 8 sensor positions that were read simultaneously. The measurement for binding was continued for the indicated time, which was followed by dipping the sensors into Buffer 1 for the indicated time to monitor the dissociation in real time. Throughout, the measurements were done at 20°C. A PBS coated sensor control was included and subtracted from all the kinetic data before quantitative analysis. Buffer 1 was 1×PBS with 0.05% Tween 20 and 0.1% BSA. The percentage of IgG remaining bound, p, was determined by using the amplitude information from both binding and dissociation curves, specifically as follows, $p=(A1+A2)/A1*100\%$, in which A1, a positive number, is the final amplitude at the end of binding measurement, and A2, a negative number as the result of dissociation, is the final amplitude at the end of dissociation measurement, as illustrated in Fig. S8A and S8B. In current study, most binding and dissociation events were measured continuously in real time for 50 min each. For experiments shown in Fig. 7, the binding and dissociation were monitored continuously for 4000 s for better definition of the rate constants.

Measurement of Ag-specific IgG concentration in animal sera using magnetic beads

We measured the concentration of Ag-specific IgG in the sera of immunized animals using streptavidin-coated magnetic beads. Specifically, high capacity Magne streptavidin beads (Promega CAT#V7820) were first exchanged into PBS buffer, and then mixed with biotinylated RBD or HEL for binding at 20°C for 1 hr with constant mixing on a lab vortexer. After this, the beads were washed 3 times using Buffer 1 and then mixed with sera also diluted in Buffer 1. The binding was continued at 20°C for 2 hrs with constant mixing. Finally, the supernatant was removed, and the bound IgG was resuspended in nonreducing Laemmli sample buffer at 95°C for 10 min. The amount of Ag-specific IgG was then quantitated by running a western blot using mouse IgG (BioLegend CAT#944803) of known mass as a standard. The secondary antibody used was goat anti-mouse IgG (Fc specific) conjugated with alkaline phosphatase from Sigma (CAT#A1418) and used at 1:3000 dilution.

Statistical analysis

Statistical analysis was carried out using the Statistics toolbox in MATLAB (Mathworks, MA). A comparison of two independent variables was carried out using a two-sample T-test. Data sets with more than two independent variables were analyzed using a one-way analysis of variance as indicated. P-values less than 0.05 were considered statistically significant. Throughout, all data points in figures were reported as mean ± standard error unless otherwise noted.

References and Notes

1. W. Cheng, The Density Code for the Development of a Vaccine? *J Pharm Sci* **105**, 3223-3232 (2016).
2. J. S. Klein, P. J. Bjorkman, Few and far between: how HIV may be evading antibody avidity. *PLoS Pathog* **6**, e1000908 (2010).
3. H. M. Dintzis, R. Z. Dintzis, B. Vogelstein, Molecular determinants of immunogenicity: the immunon model of immune response. *Proc Natl Acad Sci U S A* **73**, 3671-3675 (1976).
4. Y. Kato *et al.*, Multifaceted Effects of Antigen Valency on B Cell Response Composition and Differentiation In Vivo. *Immunity*, (2020).
5. M. F. Bachmann *et al.*, The influence of antigen organization on B cell responsiveness. *Science* **262**, 1448-1451 (1993).
6. M. F. Bachmann, R. M. Zinkernagel, Neutralizing antiviral B cell responses. *Annu Rev Immunol* **15**, 235-270 (1997).
7. F. Zabel, T. M. Kundig, M. F. Bachmann, Virus-induced humoral immunity: on how B cell responses are initiated. *Curr Opin Virol* **3**, 357-362 (2013).
8. B. Chackerian, D. R. Lowy, J. T. Schiller, Induction of autoantibodies to mouse CCR5 with recombinant papillomavirus particles. *Proc Natl Acad Sci U S A* **96**, 2373-2378 (1999).
9. B. Chackerian, D. R. Lowy, J. T. Schiller, Conjugation of a self-antigen to papillomavirus-like particles allows for efficient induction of protective autoantibodies. *J Clin Invest* **108**, 415-423 (2001).
10. B. Chackerian, M. R. Durfee, J. T. Schiller, Virus-like display of a neo-self antigen reverses B cell anergy in a B cell receptor transgenic mouse model. *J Immunol* **180**, 5816-5825 (2008).
11. M. C. Hanson *et al.*, Liposomal vaccines incorporating molecular adjuvants and intrastructural T-cell help promote the immunogenicity of HIV membrane-proximal external region peptides. *Vaccine* **33**, 861-868 (2015).
12. J. Ingale *et al.*, High-Density Array of Well-Ordered HIV-1 Spikes on Synthetic Liposomal Nanoparticles Efficiently Activate B Cells. *Cell Rep* **15**, 1986-1999 (2016).
13. K. Takeda, T. Kaisho, S. Akira, Toll-like receptors. *Annu Rev Immunol* **21**, 335-376 (2003).
14. B. Hou *et al.*, Selective utilization of Toll-like receptor and MyD88 signaling in B cells for enhancement of the antiviral germinal center response. *Immunity* **34**, 375-384 (2011).
15. A. Chaturvedi, D. Dorward, S. K. Pierce, The B cell receptor governs the subcellular location of Toll-like receptor 9 leading to hyperresponses to DNA-containing antigens. *Immunity* **28**, 799-809 (2008).
16. J. Eckl-Dorna, F. D. Batista, BCR-mediated uptake of antigen linked to TLR9 ligand stimulates B-cell proliferation and antigen-specific plasma cell formation. *Blood* **113**, 3969-3977 (2009).
17. D. C. Rookhuizen, A. L. DeFranco, Toll-like receptor 9 signaling acts on multiple elements of the germinal center to enhance antibody responses. *Proc Natl Acad Sci U S A* **111**, E3224-3233 (2014).
18. D. J. Rawlings, M. A. Schwartz, S. W. Jackson, A. Meyer-Bahlburg, Integration of B cell responses through Toll-like receptors and antigen receptors. *Nat Rev Immunol* **12**, 282-294 (2012).
19. A. Iwasaki, R. Medzhitov, Regulation of adaptive immunity by the innate immune system. *Science* **327**, 291-295 (2010).
20. A. Iwasaki, R. Medzhitov, Control of adaptive immunity by the innate immune system. *Nat Immunol* **16**, 343-353 (2015).
21. S. Hong *et al.*, B Cells Are the Dominant Antigen-Presenting Cells that Activate Naive CD4(+) T Cells upon Immunization with a Virus-Derived Nanoparticle Antigen. *Immunity* **49**, 695-708 e694 (2018).

22. Y. Takahashi, P. R. Dutta, D. M. Cerasoli, G. Kelsoe, In situ studies of the primary immune response to (4-hydroxy-3-nitrophenyl)acetyl. V. Affinity maturation develops in two stages of clonal selection. *J Exp Med* **187**, 885-895 (1998).
23. S. Han, B. Zheng, J. Dal Porto, G. Kelsoe, In situ studies of the primary immune response to (4-hydroxy-3-nitrophenyl)acetyl. IV. Affinity-dependent, antigen-driven B cell apoptosis in germinal centers as a mechanism for maintaining self-tolerance. *J Exp Med* **182**, 1635-1644 (1995).
24. J. Jacob, R. Kassir, G. Kelsoe, In situ studies of the primary immune response to (4-hydroxy-3-nitrophenyl)acetyl. I. The architecture and dynamics of responding cell populations. *J Exp Med* **173**, 1165-1175 (1991).
25. J. Jacob, G. Kelsoe, In situ studies of the primary immune response to (4-hydroxy-3-nitrophenyl)acetyl. II. A common clonal origin for periarteriolar lymphoid sheath-associated foci and germinal centers. *J Exp Med* **176**, 679-687 (1992).
26. J. Jacob, J. Przylepa, C. Miller, G. Kelsoe, In situ studies of the primary immune response to (4-hydroxy-3-nitrophenyl)acetyl. III. The kinetics of V region mutation and selection in germinal center B cells. *J Exp Med* **178**, 1293-1307 (1993).
27. J. H. Lam, N. Baumgarth, The Multifaceted B Cell Response to Influenza Virus. *J Immunol* **202**, 351-359 (2019).
28. E. Szomolanyi-Tsuda, R. M. Welsh, T-cell-independent antiviral antibody responses. *Curr Opin Immunol* **10**, 431-435 (1998).
29. L. Hangartner, R. M. Zinkernagel, H. Hengartner, Antiviral antibody responses: the two extremes of a wide spectrum. *Nat Rev Immunol* **6**, 231-243 (2006).
30. M. K. Slifka, R. Ahmed, Long-term humoral immunity against viruses: revisiting the issue of plasma cell longevity. *Trends Microbiol* **4**, 394-400 (1996).
31. A. Jegerlehner *et al.*, TLR9 signaling in B cells determines class switch recombination to IgG2a. *J Immunol* **178**, 2415-2420 (2007).
32. J. Y. Chang, K. V. Gorzelnik, J. Thongchol, J. Zhang, Structural Assembly of Qbeta Virion and Its Diverse Forms of Virus-like Particles. *Viruses* **14**, (2022).
33. B. C. Bundy, J. R. Swartz, W. Chan, Encapsidation of heterologous entities into virus-like particles. *US Patent* **US8,324,149B2**, (2010).
34. D. M. Knipe, P. M. Howley, *Fields virology*. (Wolters Kluwer/Lippincott Williams & Wilkins Health, Philadelphia, PA, ed. 6th, 2013), pp. 2 volumes.
35. M. Marchetti, G. Wuite, W. H. Roos, Atomic force microscopy observation and characterization of single virions and virus-like particles by nano-indentation. *Curr Opin Virol* **18**, 82-88 (2016).
36. D. S. Watson, A. N. Endsley, L. Huang, Design considerations for liposomal vaccines: influence of formulation parameters on antibody and cell-mediated immune responses to liposome associated antigens. *Vaccine* **30**, 2256-2272 (2012).
37. I. Yamashita, K. Iwahori, S. Kumagai, Ferritin in the field of nanodevices. *Biochim Biophys Acta* **1800**, 846-857 (2010).
38. N. P. King *et al.*, Computational design of self-assembling protein nanomaterials with atomic level accuracy. *Science* **336**, 1171-1174 (2012).
39. M. Kanekiyo *et al.*, Self-assembling influenza nanoparticle vaccines elicit broadly neutralizing H1N1 antibodies. *Nature* **499**, 102-106 (2013).
40. J. Marcandalli *et al.*, Induction of Potent Neutralizing Antibody Responses by a Designed Protein Nanoparticle Vaccine for Respiratory Syncytial Virus. *Cell* **176**, 1420-1431 e1417 (2019).
41. A. C. Walls *et al.*, Elicitation of Potent Neutralizing Antibody Responses by Designed Protein Nanoparticle Vaccines for SARS-CoV-2. *Cell* **183**, 1367-1382 e1317 (2020).

42. Z. Chen *et al.*, Self-Antigens Displayed on Liposomal Nanoparticles above a Threshold of Epitope Density Elicit Class-Switched Autoreactive Antibodies Independent of T Cell Help. *J Immunol* **204**, 335-347 (2020).
43. W. Y. Wholey *et al.*, Synthetic Liposomal Mimics of Biological Viruses for the Study of Immune Responses to Infection and Vaccination. *Bioconjug Chem* **31**, 685-697 (2020).
44. W. Y. Wholey, S. T. Yoda, W. Cheng, Site-Specific and Stable Conjugation of the SARS-CoV-2 Receptor-Binding Domain to Liposomes in the Absence of Any Other Adjuvants Elicits Potent Neutralizing Antibodies in BALB/c Mice. *Bioconjug Chem* **32**, 2497-2506 (2021).
45. T. M. Allen, P. R. Cullis, Drug delivery systems: entering the mainstream. *Science* **303**, 1818-1822 (2004).
46. D. J. Irvine, M. A. Swartz, G. L. Szeto, Engineering synthetic vaccines using cues from natural immunity. *Nat Mater* **12**, 978-990 (2013).
47. N. Pardi, M. J. Hogan, F. W. Porter, D. Weissman, mRNA vaccines - a new era in vaccinology. *Nat Rev Drug Discov* **17**, 261-279 (2018).
48. P. Zhou *et al.*, A pneumonia outbreak associated with a new coronavirus of probable bat origin. *Nature* **579**, 270-273 (2020).
49. A. Harris *et al.*, Influenza virus pleiomorphy characterized by cryoelectron tomography. *Proc Natl Acad Sci U S A* **103**, 19123-19127 (2006).
50. J. A. Briggs, T. Wilk, R. Welker, H. G. Krausslich, S. D. Fuller, Structural organization of authentic, mature HIV-1 virions and cores. *EMBO J* **22**, 1707-1715 (2003).
51. Z. Ke *et al.*, Structures and distributions of SARS-CoV-2 spike proteins on intact virions. *Nature*, (2020).
52. Z. Chen, J. J. Moon, W. Cheng, Quantitation and Stability of Protein Conjugation on Liposomes for Controlled Density of Surface Epitopes. *Bioconjug Chem* **29**, 1251-1260 (2018).
53. Y. Pang, H. Song, J. H. Kim, X. Hou, W. Cheng, Optical trapping of individual human immunodeficiency viruses in culture fluid reveals heterogeneity with single-molecule resolution. *Nat Nanotechnol* **9**, 624-630 (2014).
54. M. C. DeSantis, J. H. Kim, H. Song, P. J. Klasse, W. Cheng, Quantitative Correlation between Infectivity and Gp120 Density on HIV-1 Virions Revealed by Optical Trapping Virometry. *J Biol Chem* **291**, 13088-13097 (2016).
55. T. Junt *et al.*, Subcapsular sinus macrophages in lymph nodes clear lymph-borne viruses and present them to antiviral B cells. *Nature* **450**, 110-114 (2007).
56. T. Fehr, D. Skrastina, P. Pumpens, R. M. Zinkernagel, T cell-independent type I antibody response against B cell epitopes expressed repetitively on recombinant virus particles. *Proc Natl Acad Sci U S A* **95**, 9477-9481 (1998).
57. A. F. Ochsenbein *et al.*, Correlation of T cell independence of antibody responses with antigen dose reaching secondary lymphoid organs: implications for splenectomized patients and vaccine design. *J Immunol* **164**, 6296-6302 (2000).
58. J. F. Brooks *et al.*, Molecular basis for potent B cell responses to antigen displayed on particles of viral size,DOI 10.1038/s41590-023-01597-9. *Nat Immunol*, (2023).
59. F. Schmidt *et al.*, Measuring SARS-CoV-2 neutralizing antibody activity using pseudotyped and chimeric viruses. *J Exp Med* **217**, e20201181 (2020).
60. B. O. Lee *et al.*, CD4 T cell-independent antibody response promotes resolution of primary influenza infection and helps to prevent reinfection. *J Immunol* **175**, 5827-5838 (2005).
61. H. Tesch, F. I. Smith, W. J. Muller-Hermes, K. Rajewsky, Heterogeneous and monoclonal helper T cells induce similar anti-(4-hydroxy-3-nitrophenyl)acetyl (NP) antibody populations in the primary adoptive response. I. Isotype distribution. *Eur J Immunol* **14**, 188-194 (1984).
62. I. S. Grewal, K. D. Moudgil, E. E. Sercarz, Hindrance of binding to class II major histocompatibility complex molecules by a single amino acid residue contiguous to a

determinant leads to crypticity of the determinant as well as lack of response to the protein antigen. *Proc Natl Acad Sci U S A* **92**, 1779-1783 (1995).
63. P. Mombaerts *et al.*, Mutations in T-cell antigen receptor genes alpha and beta block thymocyte development at different stages. *Nature* **360**, 225-231 (1992).
64. B. Hou, B. Reizis, A. L. DeFranco, Toll-like receptors activate innate and adaptive immunity by using dendritic cell-intrinsic and -extrinsic mechanisms. *Immunity* **29**, 272-282 (2008).
65. R. C. Rickert, J. Roes, K. Rajewsky, B lymphocyte-specific, Cre-mediated mutagenesis in mice. *Nucleic Acids Res* **25**, 1317-1318 (1997).
66. R. C. Rickert, K. Rajewsky, J. Roes, Impairment of T-cell-dependent B-cell responses and B-1 cell development in CD19-deficient mice. *Nature* **376**, 352-355 (1995).
67. R. H. Carter, D. T. Fearon, CD19: lowering the threshold for antigen receptor stimulation of B lymphocytes. *Science* **256**, 105-107 (1992).
68. D. T. Fearon, M. C. Carroll, Regulation of B lymphocyte responses to foreign and self-antigens by the CD19/CD21 complex. *Annu Rev Immunol* **18**, 393-422 (2000).
69. D. Depoil *et al.*, CD19 is essential for B cell activation by promoting B cell receptor-antigen microcluster formation in response to membrane-bound ligand. *Nat Immunol* **9**, 63-72 (2008).
70. H. Hemmi *et al.*, A Toll-like receptor recognizes bacterial DNA. *Nature* **408**, 740-745 (2000).
71. F. Wu *et al.*, A new coronavirus associated with human respiratory disease in China. *Nature* **579**, 265-269 (2020).
72. J. M. Lund *et al.*, Recognition of single-stranded RNA viruses by Toll-like receptor 7. *Proc Natl Acad Sci U S A* **101**, 5598-5603 (2004).
73. J. J. Taylor, K. A. Pape, H. R. Steach, M. K. Jenkins, Humoral immunity. Apoptosis and antigen affinity limit effector cell differentiation of a single naive B cell. *Science* **347**, 784-787 (2015).
74. E. Szomolanyi-Tsuda, R. M. Welsh, T cell-independent antibody-mediated clearance of polyoma virus in T cell-deficient mice. *J Exp Med* **183**, 403-411 (1996).
75. M. A. Franco, H. B. Greenberg, Immunity to rotavirus in T cell deficient mice. *Virology* **238**, 169-179 (1997).
76. N. Juleff *et al.*, Foot-and-mouth disease virus can induce a specific and rapid CD4+ T-cell-independent neutralizing and isotype class-switched antibody response in naive cattle. *J Virol* **83**, 3626-3636 (2009).
77. L. C. Wang *et al.*, CD4 T-cell-independent antibody response reduces enterovirus 71 lethality in mice by decreasing tissue viral loads. *Clin Dev Immunol* **2012**, 580696 (2012).
78. J. S. Chen *et al.*, High-affinity, neutralizing antibodies to SARS-CoV-2 can be made without T follicular helper cells. *Sci Immunol* **7**, eabl5652 (2022).
79. C. L. Goodrick, Life-span and the inheritance of longevity of inbred mice. *J Gerontol* **30**, 257-263 (1975).
80. A. Bortnick *et al.*, Long-lived bone marrow plasma cells are induced early in response to T cell-independent or T cell-dependent antigens. *J Immunol* **188**, 5389-5396 (2012).
81. M. Taillardet *et al.*, The thymus-independent immunity conferred by a pneumococcal polysaccharide is mediated by long-lived plasma cells. *Blood* **114**, 4432-4440 (2009).
82. J. T. Bates *et al.*, Reversion of somatic mutations of the respiratory syncytial virus-specific human monoclonal antibody Fab19 reveal a direct relationship between association rate and neutralizing potency. *J Immunol* **190**, 3732-3739 (2013).
83. J. Foote, H. N. Eisen, Kinetic and affinity limits on antibodies produced during immune responses. *Proc Natl Acad Sci U S A* **92**, 1254-1256 (1995).
84. J. Stavnezer, J. E. Guikema, C. E. Schrader, Mechanism and regulation of class switch recombination. *Annu Rev Immunol* **26**, 261-292 (2008).
85. A. Ramiro *et al.*, The role of activation-induced deaminase in antibody diversification and chromosome translocations. *Adv Immunol* **94**, 75-107 (2007).

86. Z. Chen, J. H. Wang, Signaling control of antibody isotype switching. *Adv Immunol* **141**, 105-164 (2019).
87. Z. Xu, H. Zan, E. J. Pone, T. Mai, P. Casali, Immunoglobulin class-switch DNA recombination: induction, targeting and beyond. *Nat Rev Immunol* **12**, 517-531 (2012).
88. J. A. Roco *et al.*, Class-Switch Recombination Occurs Infrequently in Germinal Centers. *Immunity* **51**, 337-350 e337 (2019).
89. W. Liao *et al.*, Characterization of T-Dependent and T-Independent B Cell Responses to a Virus-like Particle. *J Immunol* **198**, 3846-3856 (2017).
90. T. Kaisho, F. Schwenk, K. Rajewsky, The roles of gamma 1 heavy chain membrane expression and cytoplasmic tail in IgG1 responses. *Science* **276**, 412-415 (1997).
91. C. A. Diebolder *et al.*, Complement is activated by IgG hexamers assembled at the cell surface. *Science* **343**, 1260-1263 (2014).
92. G. Trinchieri, N. Valiante, Receptors for the Fc fragment of IgG on natural killer cells. *Nat Immun* **12**, 218-234 (1993).
93. H. S. Dai *et al.*, The Fc Domain of Immunoglobulin Is Sufficient to Bridge NK Cells with Virally Infected Cells. *Immunity* **47**, 159-170 e110 (2017).
94. U. Kalinke *et al.*, The role of somatic mutation in the generation of the protective humoral immune response against vesicular stomatitis virus. *Immunity* **5**, 639-652 (1996).
95. J. H. Lam, F. L. Smith, N. Baumgarth, B Cell Activation and Response Regulation During Viral Infections. *Viral Immunol* **33**, 294-306 (2020).
96. H. P. Roost *et al.*, Early high-affinity neutralizing anti-viral IgG responses without further overall improvements of affinity. *Proc Natl Acad Sci U S A* **92**, 1257-1261 (1995).
97. R. P. Galimidi *et al.*, Intra-spike crosslinking overcomes antibody evasion by HIV-1. *Cell* **160**, 433-446 (2015).
98. M. Akkaya *et al.*, T cell-dependent antigen adjuvanted with DOTAP-CpG-B but not DOTAP-CpG-A induces robust germinal center responses and high affinity antibodies in mice. *Eur J Immunol* **47**, 1890-1899 (2017).
99. C. Pasare, R. Medzhitov, Control of B-cell responses by Toll-like receptors. *Nature* **438**, 364-368 (2005).
100. A. M. Avalos, H. L. Ploegh, Early BCR Events and Antigen Capture, Processing, and Loading on MHC Class II on B Cells. *Front Immunol* **5**, 92 (2014).
101. P. Hou *et al.*, B cell antigen receptor signaling and internalization are mutually exclusive events. *PLoS Biol* **4**, e200 (2006).
102. S. Karlin, W. Doerfler, L. R. Cardon, Why is CpG suppressed in the genomes of virtually all small eukaryotic viruses but not in those of large eukaryotic viruses? *J Virol* **68**, 2889-2897 (1994).
103. E. G. Shpaer, J. I. Mullins, Selection against CpG dinucleotides in lentiviral genes: a possible role of methylation in regulation of viral expression. *Nucleic Acids Res* **18**, 5793-5797 (1990).
104. N. A. Lind, V. E. Rael, K. Pestal, B. Liu, G. M. Barton, Regulation of the nucleic acid-sensing Toll-like receptors. *Nat Rev Immunol* **22**, 224-235 (2022).
105. C. E. Rivera *et al.*, Intrinsic B cell TLR-BCR linked coengagement induces class-switched, hypermutated, neutralizing antibody responses in absence of T cells. *Sci Adv* **9**, eade8928 (2023).
106. M. C. van Zelm *et al.*, An antibody-deficiency syndrome due to mutations in the CD19 gene. *N Engl J Med* **354**, 1901-1912 (2006).
107. M. J. Robinson *et al.*, Intrinsically determined turnover underlies broad heterogeneity in plasma-cell lifespan. *Immunity* **56**, 1596-1612 e1594 (2023).
108. M. J. Robinson *et al.*, Long-lived plasma cells accumulate in the bone marrow at a constant rate from early in an immune response. *Sci Immunol* **7**, eabm8389 (2022).
109. D. Bhattacharya, Instructing durable humoral immunity for COVID-19 and other vaccinable diseases. *Immunity* **55**, 945-964 (2022).

110. M. K. Slifka, I. J. Amanna, Role of Multivalency and Antigenic Threshold in Generating Protective Antibody Responses. *Front Immunol* **10**, 956 (2019).
111. N. Pishesha, T. J. Harmand, H. L. Ploegh, A guide to antigen processing and presentation. *Nat Rev Immunol* **22**, 751-764 (2022).
112. A. Iwasaki, Exploiting Mucosal Immunity for Antiviral Vaccines. *Annu Rev Immunol* **34**, 575-608 (2016).
113. C. B. Bridges *et al.*, Prevention and control of influenza. Recommendations of the Advisory Committee on Immunization Practices (ACIP). *MMWR Recomm Rep* **52**, 1-34; quiz CE31-34 (2003).
114. K. K. Van Rompay *et al.*, A vaccine against CCR5 protects a subset of macaques upon intravaginal challenge with simian immunodeficiency virus SIVmac251. *J Virol* **88**, 2011-2024 (2014).
115. A. Frey, J. Di Canzio, D. Zurakowski, A statistically defined endpoint titer determination method for immunoassays. *J Immunol Methods* **221**, 35-41 (1998).
116. L. Yurkovetskiy *et al.*, Structural and Functional Analysis of the D614G SARS-CoV-2 Spike Protein Variant. *Cell* **183**, 739-751 e738 (2020).
117. R. I. Connor, B. K. Chen, S. Choe, N. R. Landau, Vpr is required for efficient replication of human immunodeficiency virus type-1 in mononuclear phagocytes. *Virology* **206**, 935-944 (1995).
118. J. H. Kim, H. Song, J. L. Austin, W. Cheng, Optimized Infectivity of the Cell-Free Single-Cycle Human Immunodeficiency Viruses Type 1 (HIV-1) and Its Restriction by Host Cells. *PLoS One* **8**, e67170 (2013).
119. S. G. Arunajadai, W. Cheng, Step detection in single-molecule real time trajectories embedded in correlated noise. *PLoS One* **8**, e59279 (2013).
120. R. D. Evans, Chapter 27. *The Atomic Nucleus (McGraw-Hill)*, Chapter 27 (1969).
121. X. Hou, W. Cheng, Single-molecule detection using continuous wave excitation of two-photon fluorescence. *Optics letters* **36**, 3185-3187 (2011).
122. V. C. Coffman, J. Q. Wu, Counting protein molecules using quantitative fluorescence microscopy. *Trends Biochem Sci* **37**, 499-506 (2012).
123. J. Lawrimore, K. S. Bloom, E. D. Salmon, Point centromeres contain more than a single centromere-specific Cse4 (CENP-A) nucleosome. *J Cell Biol* **195**, 573-582 (2011).
124. A. Lu-Culligan *et al.*, No evidence of fetal defects or anti-syncytin-1 antibody induction following COVID-19 mRNA vaccination. *PLoS Biol* **20**, e3001506 (2022).

Acknowledgements:

We thank Prof. Irina Grigorova for critical reading of the work during the early development of the manuscript. We thank Prof. Marilia Cascalho for very helpful discussion regarding the data and this work. We thank Dr. Charlie Rice at Rockefeller University for the kind gift of Huh-7.5 cells. The following reagent was obtained through the AIDS Research and Reference Reagent Program, Division of AIDS, National Institute of Allergy and Infectious Diseases (NIAID), National Institutes of Health (NIH): pNL4-3.Luc.R-E- from Dr. Nathaniel Landau. The plasmid pcDNA3.1 SARS-CoV-2 S D614G was a gift from Dr. Jeremy Luban through Addgene.

Funding:

NIH/NIAID grant 1R01AI155653-01A1 (WC, JZ)

Author contributions:

Conceptualization: WC, JZ
Methodology: WW, ARM, SY, BC, WC
Investigation: WW, ARM, SY, WC
Visualization: WW, ARM, WC
Funding acquisition: WC, JZ
Project administration: WC
Supervision: WC
Writing: WW, ARM, BC, JZ, WC

Competing interests

W. Cheng has a patent pending on SVLS. B. Chackerian has equity in Flagship Laboratories 72. J. Zikherman is on the scientific advisory board for Walking Fish Therapeutics. No other disclosures were reported.

Data and materials availability:

All data are available in the main text or the supplementary materials.

Supplementary Materials

Figs. S1 to S9
Tables S1 to S5

Figures

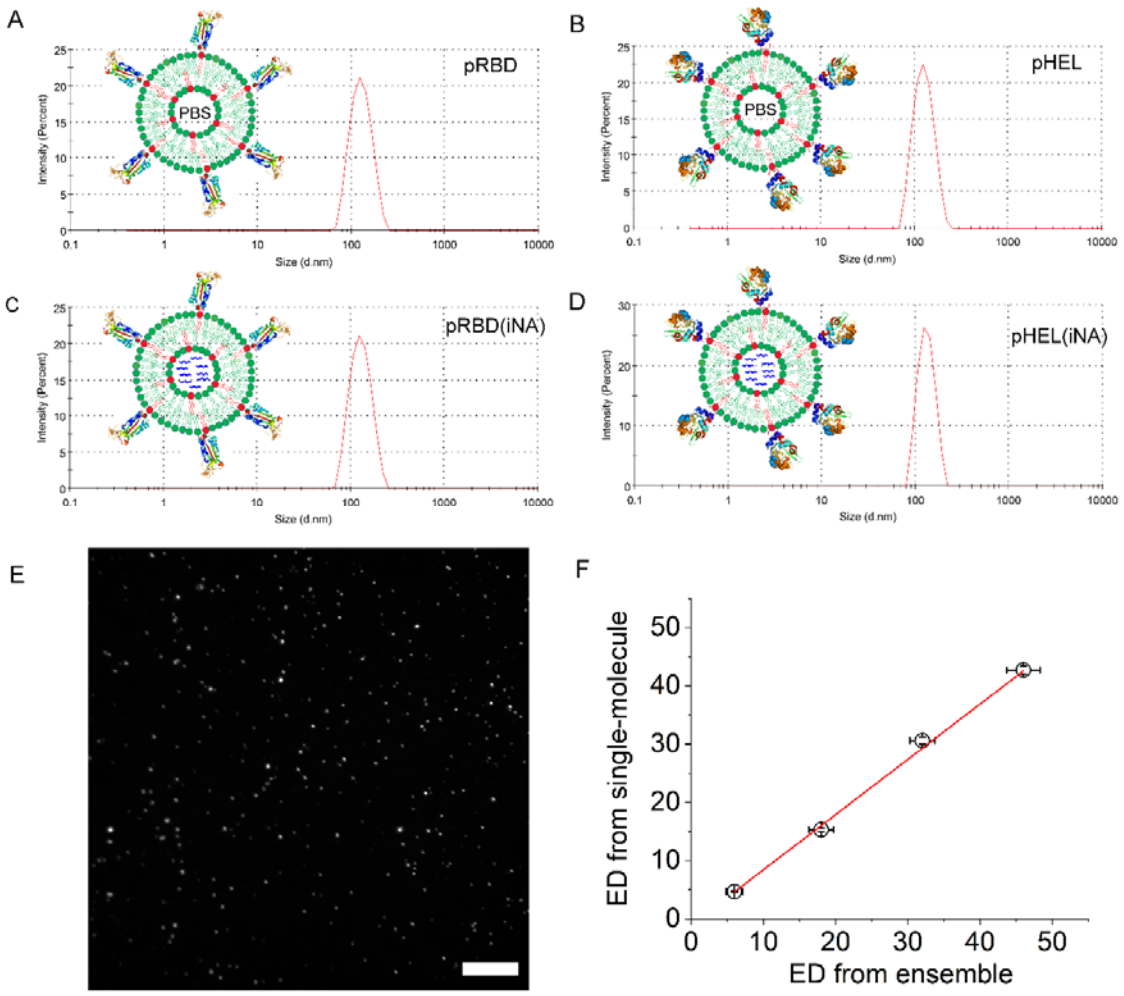

Fig. 1. Characterization of SVLS that quantitatively incorporate the common consensus features of enveloped viruses. (**A**) through (**D**): representative intensity distributions of particle sizes measured using dynamic light scattering for four types of SVLS, schematically shown as insets in each panel. The structure surface is conjugated with RBD (A, C) or HEL (B, D) site-specifically at regulated average spatial densities. The internal space of the structures is either PBS for investigation of ED in isolation (A, B) or loaded with nucleic acids to study the effects of iNA (C, D). The average diameters together with PDI values are 122 nm, 0.037 for a pRBD; 120 nm, 0.039 for a pHEL; 123 nm, 0.042 for a pRBD(DNA1); and 124 nm, 0.054 for a pHEL(DNA1). Cartoon insets adapted from (*43*, *44*). (**E**) A representative epi-fluorescence image of individual SVLS on a poly-L-lysine coated coverslip stained by a fluorescent Fab (Fig. S1). The scale bar represents 10 µm. (**F**) Correlation between ED measured using single-molecule fluorescence technique (Fig. S1) and the ensemble technique for a set of pRBD(DNA1).

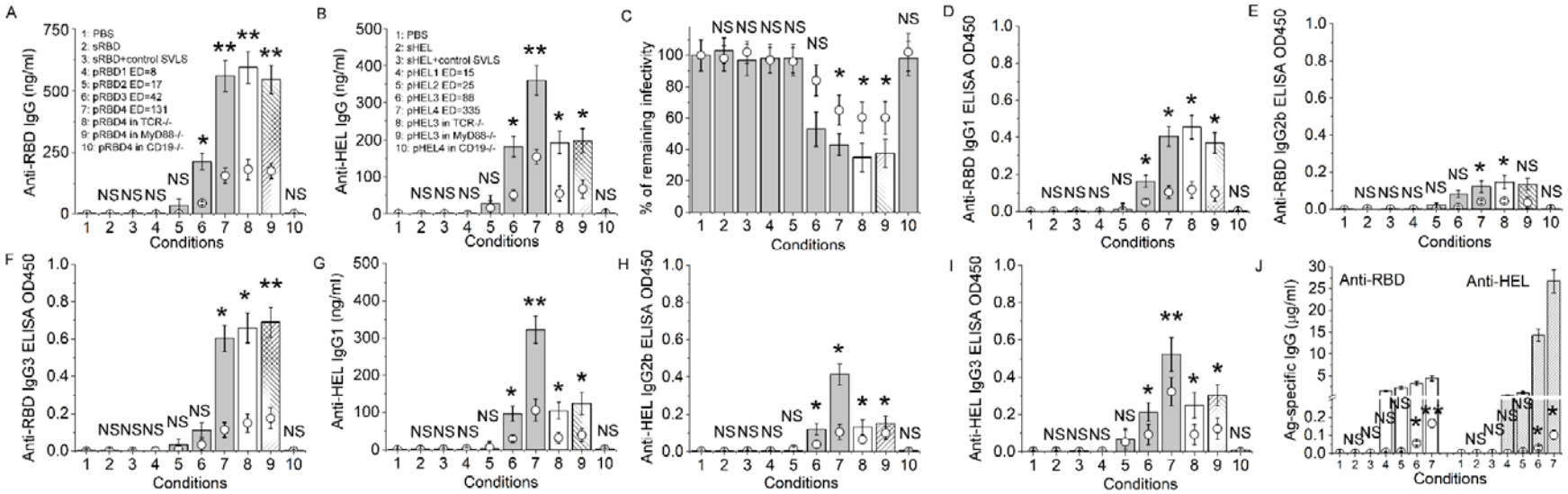

Fig. 2. Rapid IgG responses induced by SVLS without iNA. (**A**)(**B**) RBD-specific IgG (A) or HEL-specific IgG (B) in mouse sera of B6 genetic background measured by ELISA after a single injection using various agents listed in the insets. (**C**) Neutralization of HIV-1 virions pseudotyped with SARS-CoV-2 S protein by mouse sera. (**D**) through (**I**): ELISA detection for RBD- and HEL-specific IgG subclasses in sera samples from (A) and (B). The y-axes for panels (D), (E), (F), (H) and (I) are shown in OD450 for 100-fold diluted sera because reference Ag-specific IgG subclasses are not available. (**J**) RBD-specific IgG (left) or HEL-specific IgG (right) in BALB/c mouse sera measured by ELISA after a single injection using various agents #1 through #7 as listed in (A) and (B) insets. Throughout Fig. 2, data from D5 post immunization are shown in circles and D11 are shown in columns; the doses of RBD and HEL were 0.24 and 0.3 μg per animal, respectively for Conditions 2 through 10. The pairwise statistical difference between each condition and Condition 1 on Day 5 was determined by Student's T-test and shown using the following set of symbols; **: p-value < 0.01; *: p-value < 0.05; NS: not significant, p-value > 0.05. N=4.

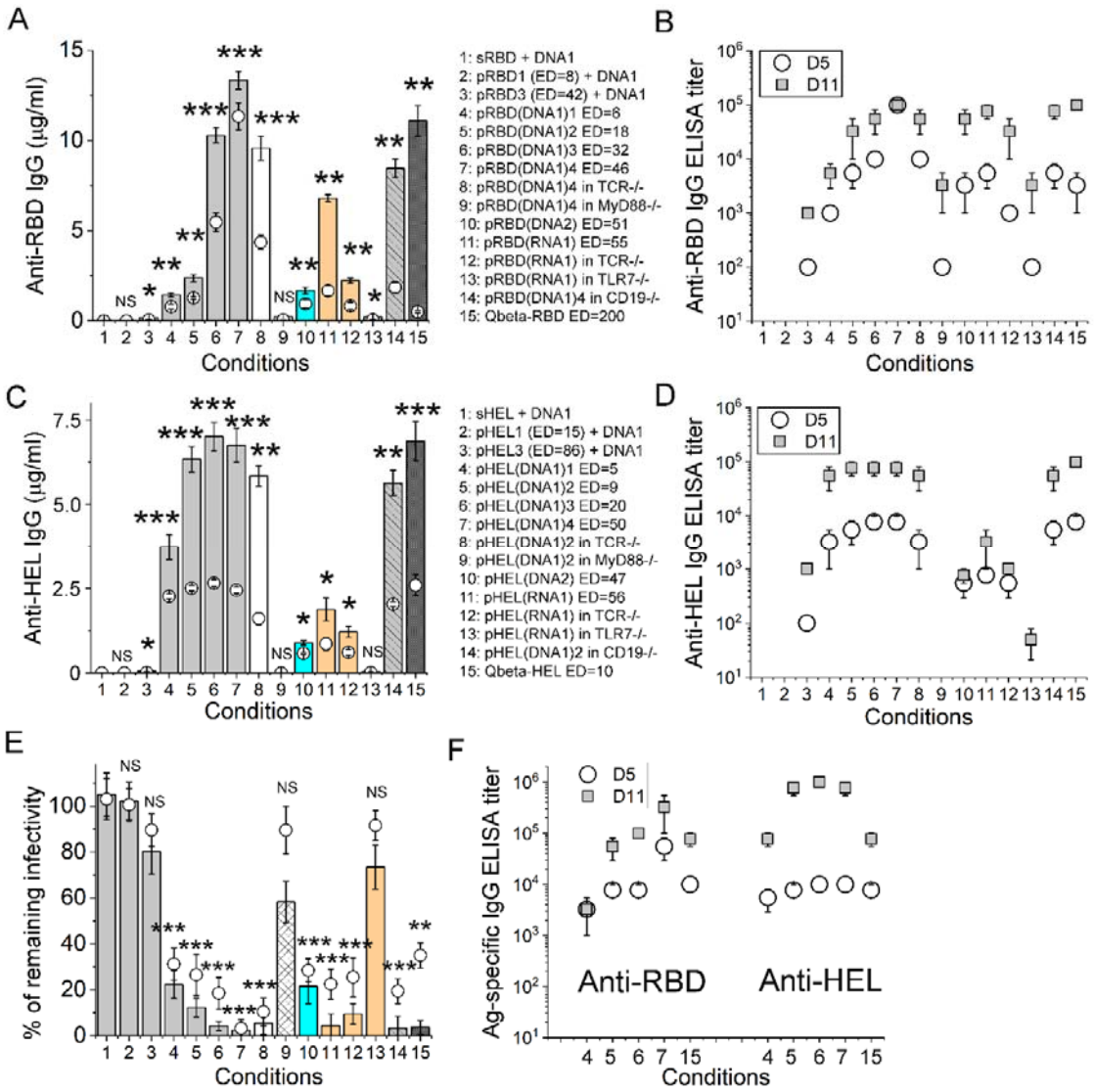
A
Anti-RBD IgG (µg/ml)
Conditions
1: sRBD + DNA1
2: pRBD1 (ED=8) + DNA1
3: pRBD3 (ED=42) + DNA1
4: pRBD(DNA1)1 ED=6
5: pRBD(DNA1)2 ED=18
6: pRBD(DNA1)3 ED=32
7: pRBD(DNA1)4 ED=46
8: pRBD(DNA1)4 in TCR-/-
9: pRBD(DNA1)4 in MyD88-/-
10: pRBD(DNA2) ED=51
11: pRBD(RNA1) ED=55
12: pRBD(RNA1) in TCR-/-
13: pRBD(RNA1) in TLR7-/-
14: pRBD(DNA1)4 in CD19-/-
15: Qbeta-RBD ED=200
B
Anti-RBD IgG ELISA titer
D5
D11
Conditions
C
Anti-HEL IgG (µg/ml)
Conditions
1: sHEL + DNA1
2: pHEL1 (ED=15) + DNA1
3: pHEL3 (ED=86) + DNA1
4: pHEL(DNA1)1 ED=5
5: pHEL(DNA1)2 ED=9
6: pHEL(DNA1)3 ED=20
7: pHEL(DNA1)4 ED=50
8: pHEL(DNA1)2 in TCR-/-
9: pHEL(DNA1)2 in MyD88-/-
10: pHEL(DNA2) ED=47
11: pHEL(RNA1) ED=56
12: pHEL(RNA1) in TCR-/-
13: pHEL(RNA1) in TLR7-/-
14: pHEL(DNA1)2 in CD19-/-
15: Qbeta-HEL ED=10
D
Anti-HEL IgG ELISA titer
D5
D11
Conditions
E
% of remaining infectivity
Conditions
F
Ag-specific IgG ELISA titer
D5
D11
Anti-RBD
Anti-HEL
Conditions

Fig. 3. Strong and rapid IgG responses induced by SVLS with various iNA. (**A**) and (**C**) ELISA measurements for RBD-specific IgG (A) or HEL-specific IgG (C) in B6 genetic background after a single injection using various agents listed in respective insets. (**B**) and (**D**) Titers for RBD-specific IgG (B) or HEL-specific IgG (D) measured for various conditions as in (A) and (C). (**E**) Neutralization of HIV-1 virions pseudotyped with SARS-CoV-2 S protein by mouse sera from various conditions in (A). (**F**) Titer values for RBD-specific IgG (left) or HEL-specific IgG (right) in BALB/c mice after a single injection using agents #4, 5, 6, 7 and 15 as listed in (A) and (C) insets. Throughout Fig. 3, data from D5 post immunization are shown in circles and D11 are shown in columns or squares; the doses of RBD and HEL were 0.24 and 0.1 μg per animal, respectively for Conditions 2 through 15; the pairwise statistical difference between each condition and Condition 1 on Day 5 was determined by Student's T-test and shown using the following set of symbols; ***: p-value < 0.001; **: p-value < 0.01; *: p-value < 0.05; NS: not significant, p-value > 0.05. N=4.

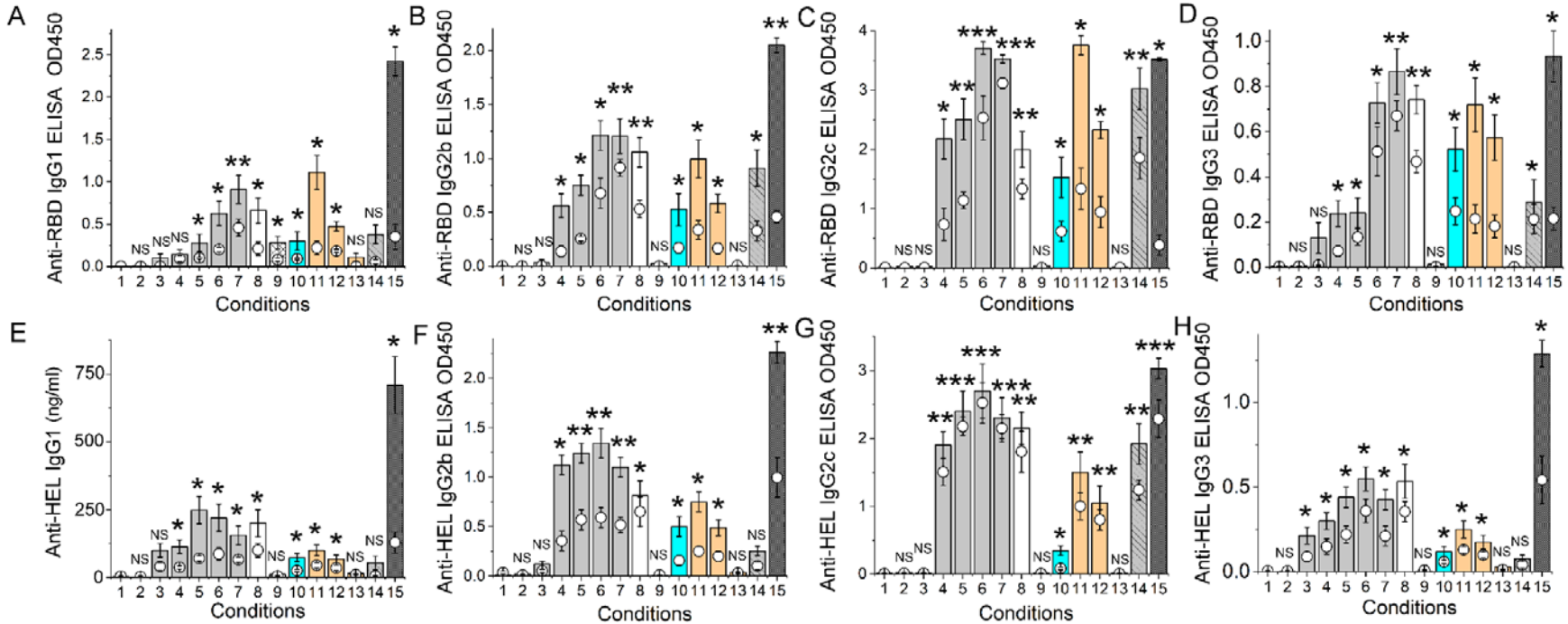

Fig. 4. Ag-specific IgG subclasses induced by SVLS with various iNA. ELISA OD values for RBD-specific (A through D) and HEL-specific (F through H) IgG subclasses for sera from conditions listed in Fig. 3A and 3C, respectively. Sera were diluted 100-fold for all. For panel E, the availability of mAb2 (Fig. S2) allowed us to estimate the concentration of anti-HEL IgG1 in mouse sera, which is plotted along the y axis. Throughout Fig. 4, data from D5 post immunization are shown in circles and D11 are shown in columns. The pairwise statistical difference between each condition and Condition 1 on Day 5 was determined by Student's T-test and shown using the following set of symbols; ***: p-value < 0.001; **: p-value < 0.01; *: p-value < 0.05; NS: not significant, p-value > 0.05. N=4.

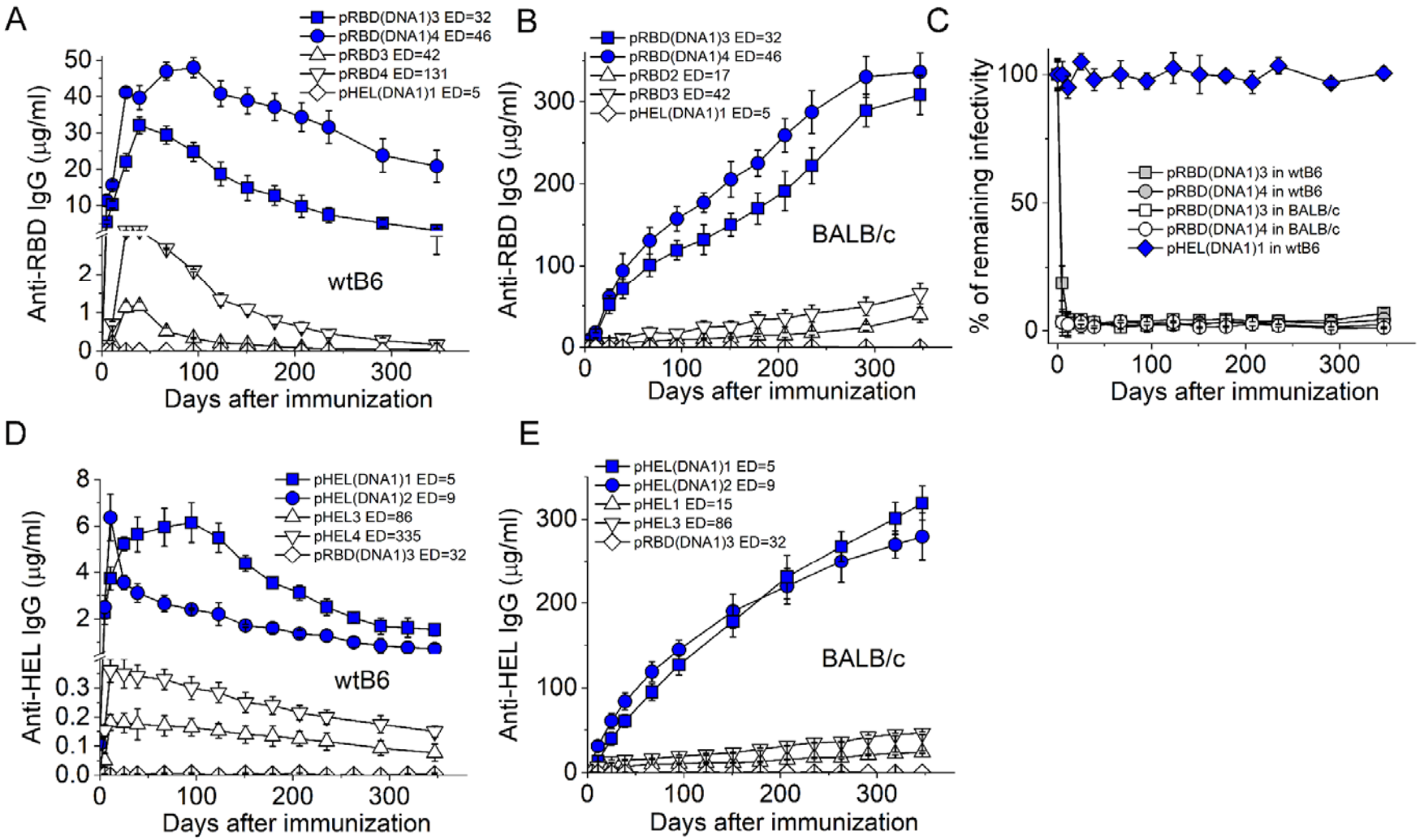
A
pRBD(DNA1)3 ED=32
pRBD(DNA1)4 ED=46
pRBD3 ED=42
pRBD4 ED=131
pHEL(DNA1)1 ED=5
Anti-RBD IgG (μg/ml)
wtB6
Days after immunization
B
pRBD(DNA1)3 ED=32
pRBD(DNA1)4 ED=46
pRBD2 ED=17
pRBD3 ED=42
pHEL(DNA1)1 ED=5
Anti-RBD IgG (μg/ml)
BALB/c
Days after immunization
C
% of remaining infectivity
pRBD(DNA1)3 in wtB6
pRBD(DNA1)4 in wtB6
pRBD(DNA1)3 in BALB/c
pRBD(DNA1)4 in BALB/c
pHEL(DNA1)1 in wtB6
Days after immunization
D
pHEL(DNA1)1 ED=5
pHEL(DNA1)2 ED=9
pHEL3 ED=86
pHEL4 ED=335
pRBD(DNA1)3 ED=32
Anti-HEL IgG (μg/ml)
wtB6
Days after immunization
E
pHEL(DNA1)1 ED=5
pHEL(DNA1)2 ED=9
pHEL1 ED=15
pHEL3 ED=86
pRBD(DNA1)3 ED=32
Anti-HEL IgG (μg/ml)
BALB/c
Days after immunization

Fig. 5. Duration of the IgG response induced by SVLS. (**A**)(**B**) and (**D**)(**E**) Concentrations of Ag-specific IgG in mouse sera collected on different days after a single injection of various agents listed in each inset. All concentrations were measured using ELISA based on standard curves obtained from mAb1 or mAb2 (Fig. S2). (**C**) Time courses of pseudovirion neutralization by various sera from immunized animals as listed in the inset. The dose of Ags for SVLS(iNA) were the same as indicated in Fig. 3 legend. The dose of Ags for SVLS without iNA were the same as indicated in Fig. 2 legend.

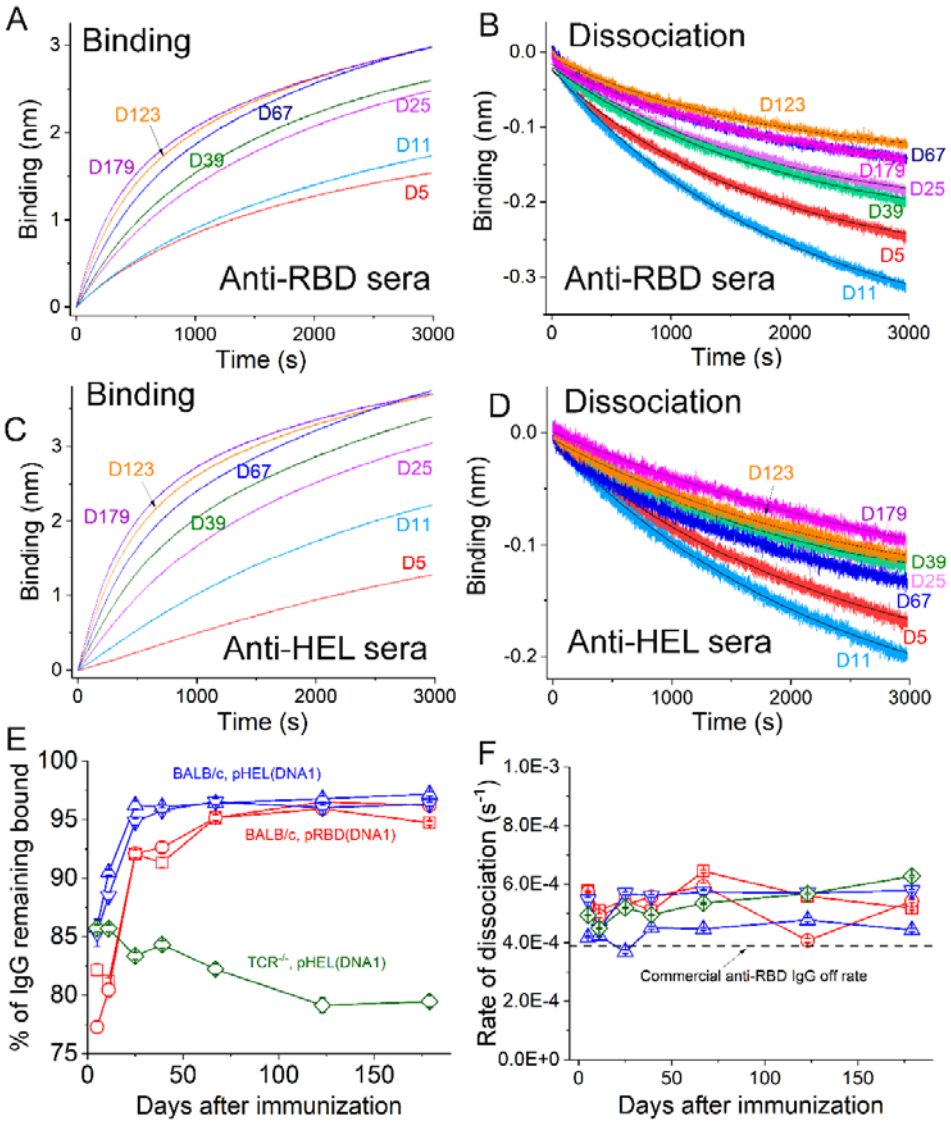

Fig. 6. Kinetics for the binding and dissociation of Ag-specific IgG induced by SVLS monitored using BioLayer interferometry. (**A**)(**B**)(**C**) and (**D**) Real-time binding and dissociation measurements for mouse sera from different days after immunization using BioLayer interferometry. (**E**)(**F**), percent of IgG remaining bound at the end of dissociation (E) and the dissociation rates (F) as a function of days after immunization measured using BioLayer interferometry for sera samples from various immunization conditions as indicated in (E). For both (E) and (F), red squares, red circles, upper triangles, down triangles and diamonds represent sera samples from immunizations using pRBD(DNA1)3, pRBD(DNA1)4, pHEL(DNA1)1, pHEL(DNA1)2, and pHEL(DNA1)1 respectively. The doses of RBD and HEL were 0.24 and 0.1 µg per animal, respectively.

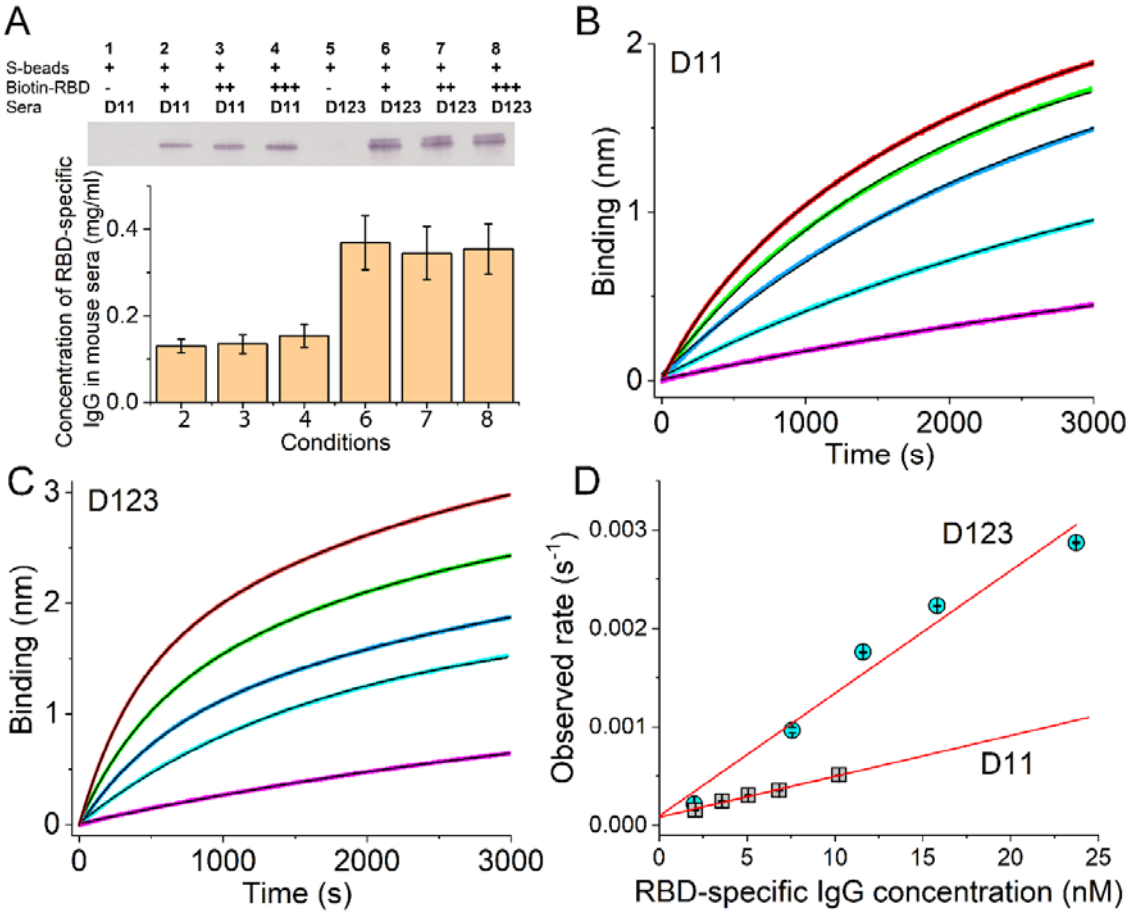

Fig. 7. Affinity maturation of the RBD-specific IgG response induced by pRBD(DNA1) in BALB/c mice. (**A**) RBD-specific IgG capture using streptavidin-coated magnetic beads together with biotin-RBD. (**B**)(**C**) Real-time binding curves between biotin-RBD and mouse sera at various dilutions, with (B) for sera collected on D11 and (C) for sera collected on D123 after the single injection. The dose of RBD was 0.24 µg per animal. The concentrations of RBD-specific IgG in each dilution are shown in panel (D) along the x-axis. The exponential fits are shown in black solid curves. (**D**) The observed binding rate constants obtained from exponential fits of the binding curves shown in (B) and (C) are plotted as a function of RBD-specific IgG concentration for sera from D11 (grey squares) and sera from D123 (cyan circles). Adjusted R-square values from linear regressions are 0.987 for D11 and 0.960 for D123, respectively.

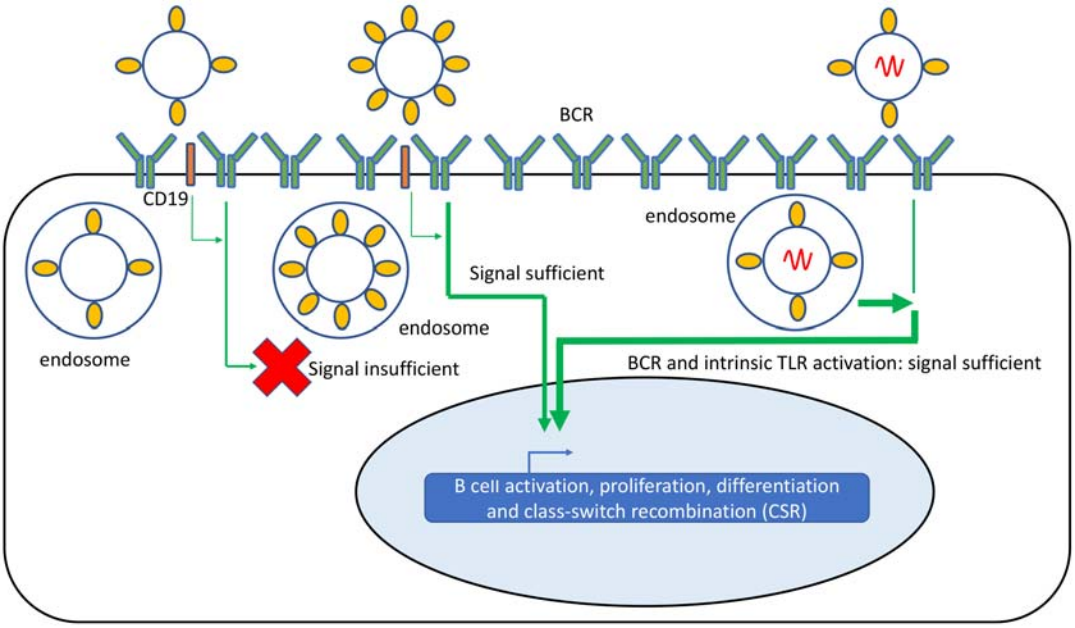

Fig. 8. Illustration of signaling threshold required for CSR and IgG secretion in Ag-specific B cells upon recognition of virus-like Ags *in vivo*. BCR-mediated endocytosis can occur to all particles depicted above, from low to high ED. However, for SVLS without iNA, both CD19 and a threshold of ED are required to meet the signaling threshold required for CSR and IgG secretion. For SVLS with iNA, CD19 can be bypassed for CSR and IgG secretion because the combined signal from BCR and intrinsic TLR activation can be sufficient to overcome the signaling threshold. Note that BCR and intrinsic TLR activation converge at or before CSR and IgG secretion take place. In response to virus-like Ags, CSR and IgG secretion can occur independently of cognate T-cell help or TLR activation. Also, Ag-specific B cells may undergo proliferation and/or differentiation before CSR and IgG secretion, which is noted above.

Supplementary Materials for

Minimal determinants for durable B cell antibody response towards virus-like antigens

Wei-Yun Wholey[1†], Alexander R. Meyer[1†], Sekou-Tidiane Yoda[1], Bryce Chackerian[2], Julie Zikherman[3]*, Wei Cheng[1,4]*

[1]*Department of Pharmaceutical Sciences, 428 Church Street, University of Michigan, Ann Arbor, Michigan 48109, USA*

[2]*Department of Molecular Genetics and Microbiology, School of Medicine, University of New Mexico, Albuquerque, New Mexico 87131, USA*

[3]*Division of Rheumatology, Rosalind Russell and Ephraim P. Engleman Rheumatology Research Center, Department of Medicine, University of California, San Francisco, California 94143 USA*

[4]*Department of Biological Chemistry, 1150 W. Medical Center Dr., University of Michigan Medical School, Ann Arbor, Michigan 48109, USA*

*Correspondence to: julie.zikherman@ucsf.edu; chengwe@umich.edu

This PDF file includes:

Figs. S1 to S9

Tables S1 to S5

Fig. S1. Characterization of RBD-conjugated SVLS using a single-molecule fluorescence approach.

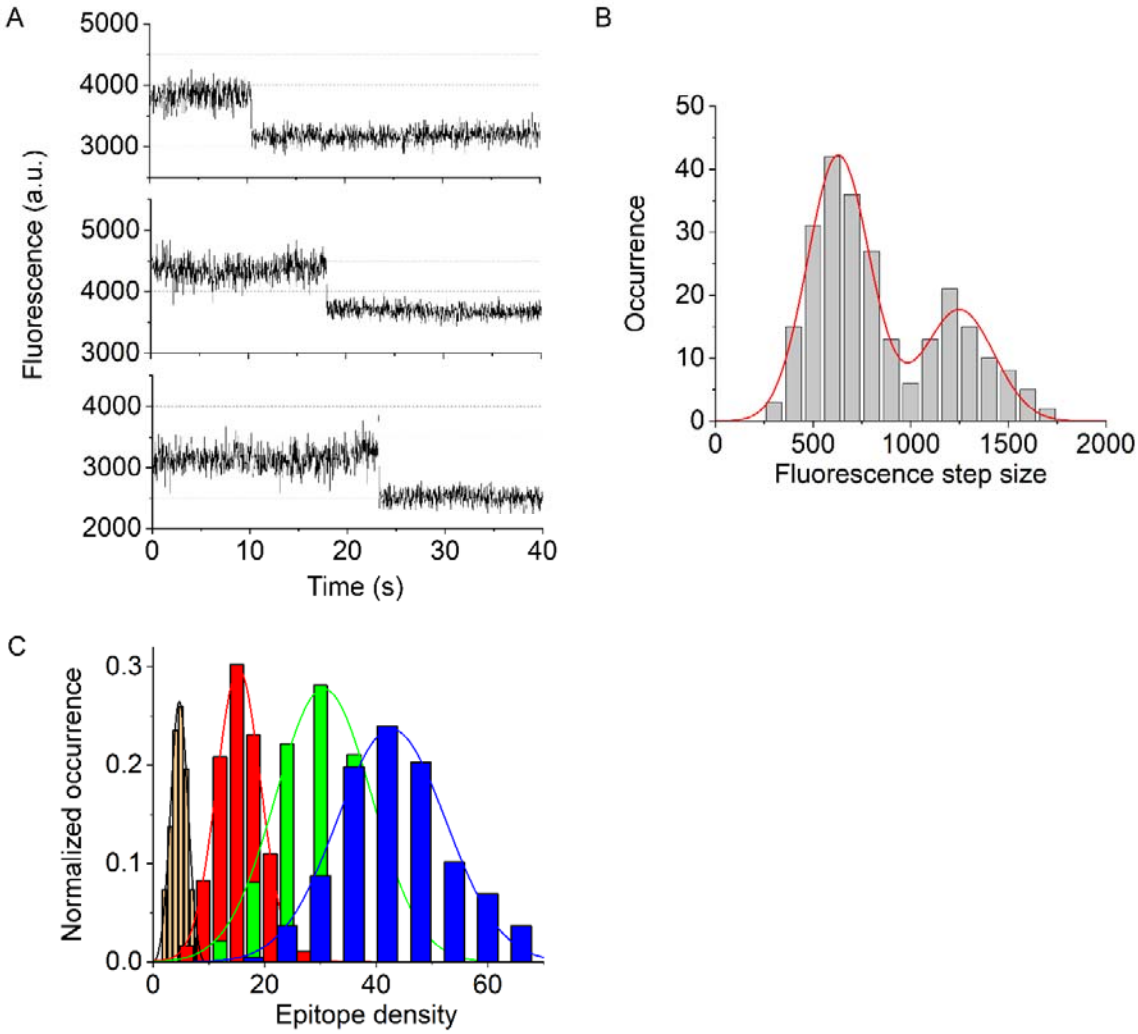

(**A**) Representative single-molecule fluorescence trajectories from Alexa-594 labeled RBD-specific Fab (Alexa-594-Fab). We prepared Alexa-594-Fab using a monoclonal IgG2a specific for SARS-CoV-2 RBD (BioLegend #944803, mAb1 herein). This high-affinity Fab allowed us to quantitate epitope density (ED) on individual SVLS conjugated with RBD, using single-molecule fluorescence techniques that we established previously (*52-54*). Briefly, the Fab was prepared from the IgG form of the antibody using a Pierce™ Fab Micro preparation kit (ThermoFisher Scientific, CAT#44685) following manufacturer instructions. The purified Fab was then labeled using Alexa Fluor 594 succinimidyl NHS ester (ThermoFisher Scientific, CAT#A37572) following the protocol that we established previously (*53*). The labeling ratio between the dye and protein was determined to be 3.3 dye molecules per Fab based on single-molecule two-photon fluorescence measurement as we described previously (*53*). As shown in Fig. 1E in the main text, we deposited pRBD(DNA1)4 bound with Alexa-594-Fab on poly-L-lysine coated coverslips and used epi-fluorescence imaging to directly visualize individual SVLS through excitation of the Alexa-594 fluorophore by a 592-nm laser. Individual SVLS showed up as bright spots in a dark

background. Neither SVLS alone nor free Alexa-594-Fab alone at the same concentrations yielded these bright spots under the microscope. Moreover, no fluorescent spots were visible when Alexa-594-Fab was incubated with control SVLS without RBD conjugation, confirming that these fluorescent spots were specific for SVLS conjugated with RBD but not protein aggregates. In order to determine the number of RBD molecules per SVLS, we chose to work at a laser power of 100 mW. This illumination condition allowed us to collect the initial fluorescence intensity from individual spots, and the constant illumination of the sample under this condition also allowed us to observe the photobleaching of individual fluorophores with time. As shown in Fig. S1A, these photobleaching events display a hallmark feature of 'steps', where the fluorescence persists for a finite time followed by a sudden decrease in fluorescence intensity. These steps correspond to the photobleaching of individual molecules. We have used a step-detection algorithm that we developed previously (*119*) to identify steps from these real-time fluorescence traces. Measurement of this 'step' size yields the fluorescence intensity of a single Alexa-594 fluorophore, which can be used as an internal reference to convert the initial fluorescence intensity of individual liposomes to the number of Alexa-594 fluorophores, as we have done previously for individual HIV-1 virions (*54*) and individual protein-conjugated liposomes (*52*) using the same quantitation methodology. (**B**) The histogram of the individual photobleaching step sizes for Alexa-594 molecules (N=247), which could be well described by the sum of two Gaussians (red curve), one centered at 630 ± 15 analog-to-digital units (a.u., mean ± standard error) and the other centered at 1249 ± 40 a.u. Under a statistical significance level of 5%, Pearson's Chi-square test (*120*) selected the double-Gaussian distribution (P-value=0.88) and rejected the single-Gaussian distribution (P-value=0.02) as the model to describe the data. The difference in peak values is close to twofold. As we have observed previously, the secondary peak may result from the photobleaching of two Alexa-594 molecules that occurred almost simultaneously, which could not be resolved by either the finite camera exposure time or the step-finding algorithm (*53, 121*). The fluorescence intensity of a single Alexa-594 fluorophore can then be used to calculate the total number of Alexa-594 molecules per SVLS based on a ratio comparison (*122, 123*) with the initial fluorescence intensity of Alexa-594 associated with individual SVLS. The number of RBD molecules per SVLS was then calculated as the total number of Alexa-594 molecules per SVLS normalized by the average number of Alexa-594 molecules per Fab. (**C**) The distributions of ED for pRBD(DNA1)1 (orange), pRBD(DNA1)2 (red), pRBD(DNA1)3 (green), and pRBD(DNA1)4 (blue). These distributions can be well described with Gaussian probability density function, with means and standard deviations of 5 ± 2 for pRBD(DNA1)1 (N=204), 15 ± 4 for pRBD(DNA1)2 (N=182), 31 ± 9 for pRBD(DNA1)3 (N=185), and 43 ± 10 for pRBD(DNA1)4 (N=217), respectively. These values are very close to the value of ED estimated using the ensemble approach as we established previously (Fig. 1F) (*42-44, 52*).

Fig. S2. A representative set of standard curves for ELISA obtained using purified mouse monoclonal antibodies.

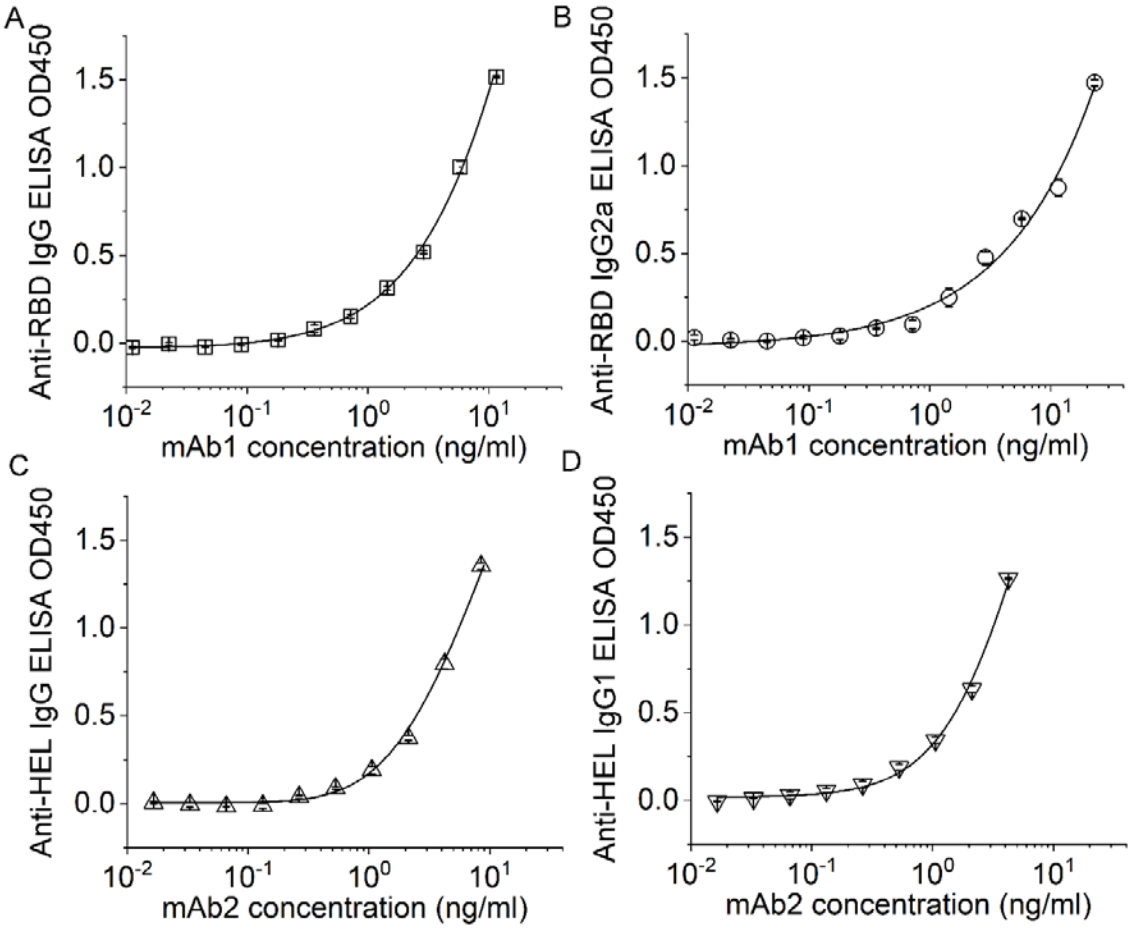

(A) and (B) We used mAb1, the commercial RBD-specific monoclonal mouse IgG2a (BioLegend CAT#944803) as the known reference to construct standard curves for ELISA to indicate the sensitivity of current ELISA assays for detection of RBD-specific IgG and IgG2a. (C) and (D) We used mAb2, the HEL-specific monoclonal mouse IgG1 (clone HyHEL10, a special gift from Prof. Irina Grigorova) as the known reference to construct standard curves for ELISA to indicate the sensitivity of current ELISA assays for detection of HEL-specific IgG and IgG1. The results are representative of three or more independent repeats of the same experiments. The data were all fit to Richard's five-parameter dose-response curves (black curves throughout Fig. S2) in GraphPad Prism 9 for interpolation of Ag-specific IgG concentrations (*124*).

Fig. S3. IgG2c was below the limit of detection in mice of B6 genetic background upon a single subcutaneous injection of SVLS without iNA.

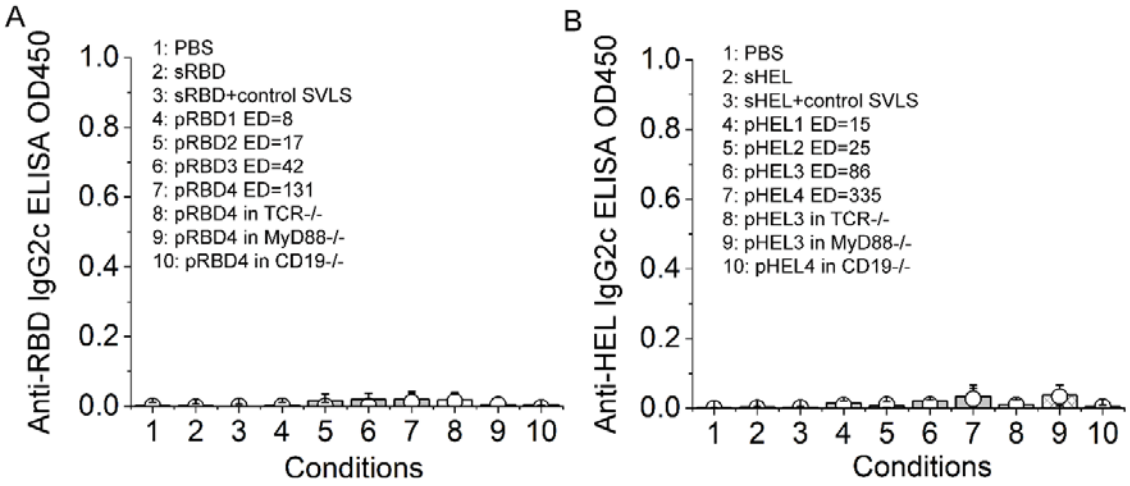

(**A**) ELISA OD values for RBD-specific IgG2c antibody from 1:100 diluted mouse sera after a single subcutaneous injection using various agents listed in the inset with no additional adjuvant. The dose of RBD was 0.24 µg per animal for Conditions 2 through 10. ED refers to epitope density. (**B**) ELISA OD values for HEL-specific IgG2c antibody from 1:100 diluted mouse sera after a single inoculation using various agents listed in the inset. The dose of HEL was 0.3 µg per animal for Conditions 2 through 10. Sera from Day 5 are shown in circles and those from Day 11 post immunization are shown in columns. Graphs depict N=4 mice and are representative of two independent experiments. Throughout Fig. S3, Conditions 1 through 7 were for wtB6 mice. Conditions 8 through 10 were for gene knockout mice of B6 genetic background, with Condition 8 as $TCR^{-/-}$, Condition 9 as $MyD88^{-/-}$ and Condition 10 as $CD19^{-/-}$, following the descriptions in the main text. The pairwise statistical difference between Condition 1 and others on Day 5 was determined by Student's T-test and none of the conditions shows statistical significance, with p-value > 0.05. Error bars represent the standard errors (N=4).

Fig. S4. Ag-specific IgG subclasses in BALB/c mice upon a single subcutaneous injection of SVLS without iNA.

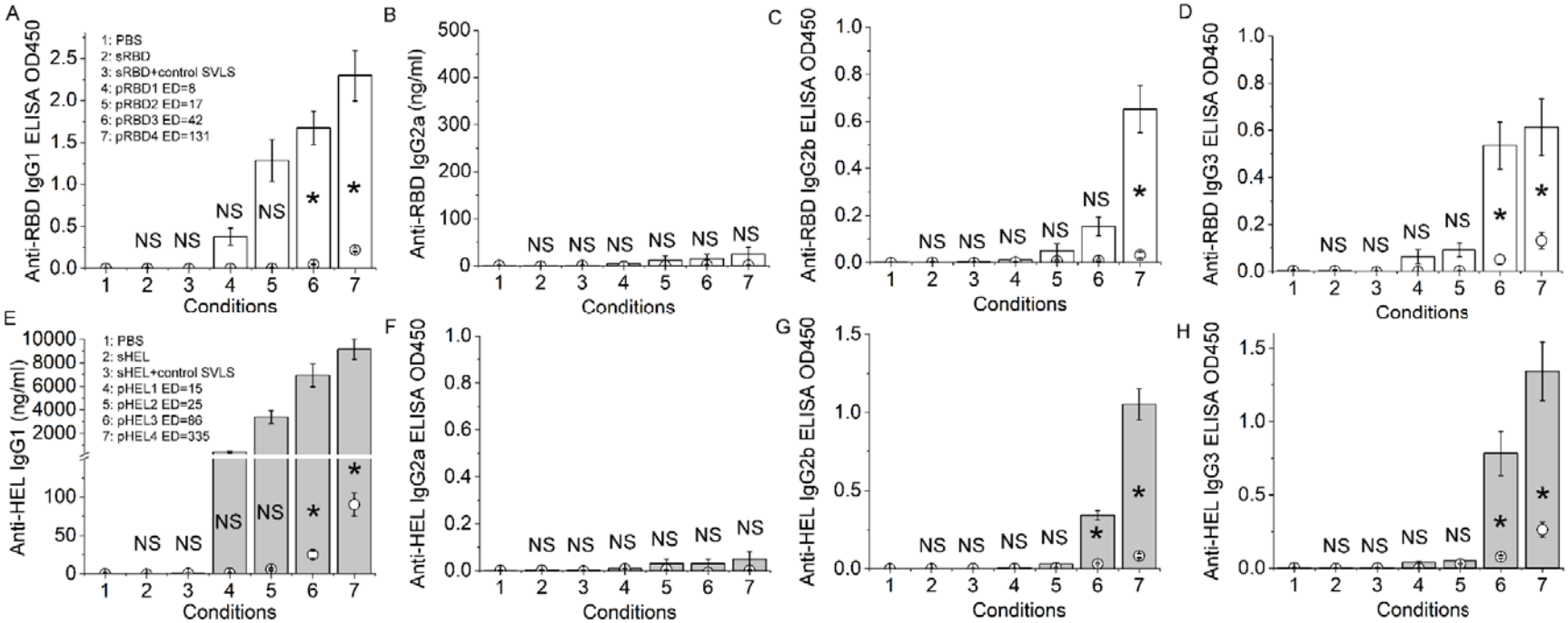

(**A**) through (**D**) ELISA measurements for RBD-specific IgG1 (A), IgG2a (B), IgG2b (C), and IgG3 (D) in mouse sera after a single subcutaneous injection using various agents listed in (A) inset with no additional adjuvant. The dose of RBD per injection was 0.24 µg for conditions 2 through 7. (**E**) through (**H**) ELISA measurements for HEL-specific IgG1 (E), IgG2a (F), IgG2b (G) and IgG3 (H) in mouse sera after a single subcutaneous injection using various agents listed in (E) inset with no additional adjuvant. The dose of HEL per injection was 0.3 µg for conditions 2 through 7. Throughout Fig. S4, data from D5 post immunization shown in circles and D11 shown in columns. The pairwise statistical difference between each condition and Condition 1 on Day 5 was determined by Student's T-test and shown using the same set of symbols as Fig. 2. N=4. The y-axes for panels (A), (C), (D), (F), (G) and (H) are shown in OD450 for 100-fold diluted sera because reference Ag-specific IgG subclasses are not available.

Fig. S5. Ag-specific IgG subclasses in BALB/c mice upon a single subcutaneous injection of pRBD(DNA1), pHEL(DNA1) or Qβ conjugates.

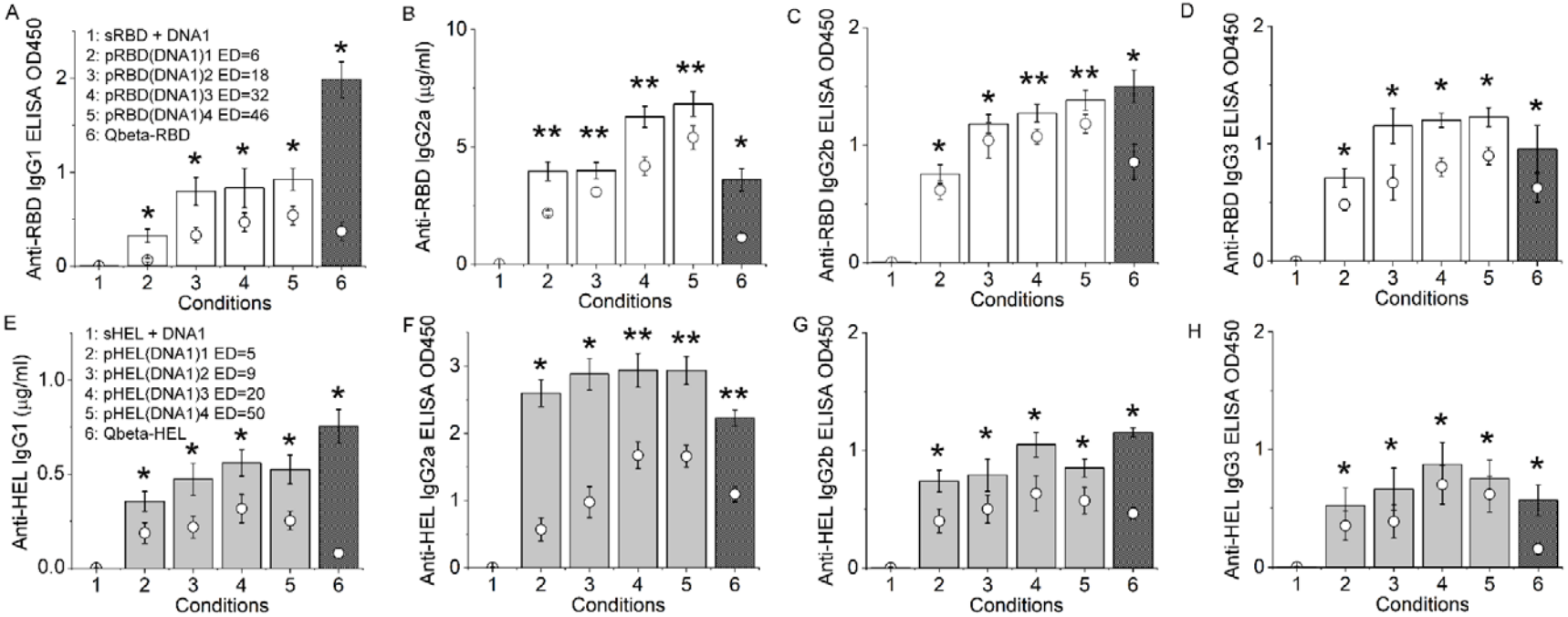

(**A**) through (**D**) ELISA measurements for RBD-specific IgG1 (A), IgG2a (B), IgG2b (C) and IgG3 (D) antibody from 1:100 diluted mouse sera after a single subcutaneous injection using various agents listed in (A) inset with no additional adjuvant. For panel B, the availability of mAb1 (Fig. S2) allowed us to estimate the concentration of anti-RBD IgG2a in mouse sera, which is plotted along the y axis. The dose of RBD per injection was 0.24 μg for conditions 1 through 6. (**E**) through (**H**) ELISA measurements for HEL-specific IgG1 (E), IgG2a (F), IgG2b (G) and IgG3 (H) antibody from 1:100 diluted mouse sera after a single subcutaneous injection using various agents listed in (E) inset with no additional adjuvant. For panel E, the availability of mAb2 (Fig. S2) allowed us to estimate the concentration of anti-HEL IgG1 in mouse sera, which is plotted along the y axis. The dose of HEL per injection was 0.1 μg for conditions 1 through 6. Throughout Fig. S5, data from D5 post immunization shown in circles and D11 shown in columns. The pairwise statistical difference between each condition and Condition 1 on Day 5

was determined by Student's T-test and shown using the same set of symbols as Fig. 2. Error bars represent the standard errors (N=4). The dose of DNA1 in the admixture with soluble proteins was 1 nmol.

Fig. S6. Life-long nAb responses induced by pRBD(DNA1) in BALB/c mice.

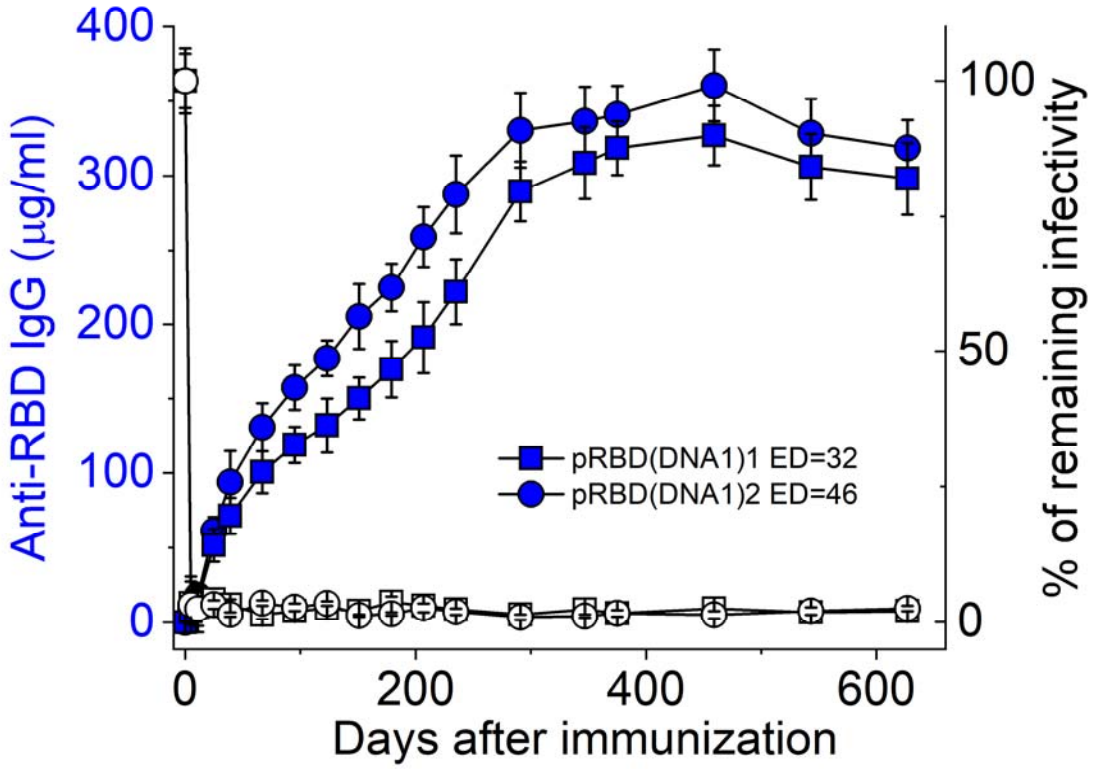

Left y-axis and blue solid symbols: Concentrations for RBD-specific IgG as measured from ELISA for mouse sera collected on different days after a single injection of the respective agents in BALB/c mice as listed in the inset. **Right y-axis and white symbols**: time courses of pseudovirion neutralization by mouse sera from BALB/c mice after a single injection of the agents listed in the inset, with white squares for pRBD(DNA1)3 (ED=32) and white circles for pRBD(DNA1)4 (ED=46). The doses of RBD were 0.24 μg per animal.

Fig. S7. Validation of low-density coating of streptavidin sensors in BioLayer interferometry experiments.

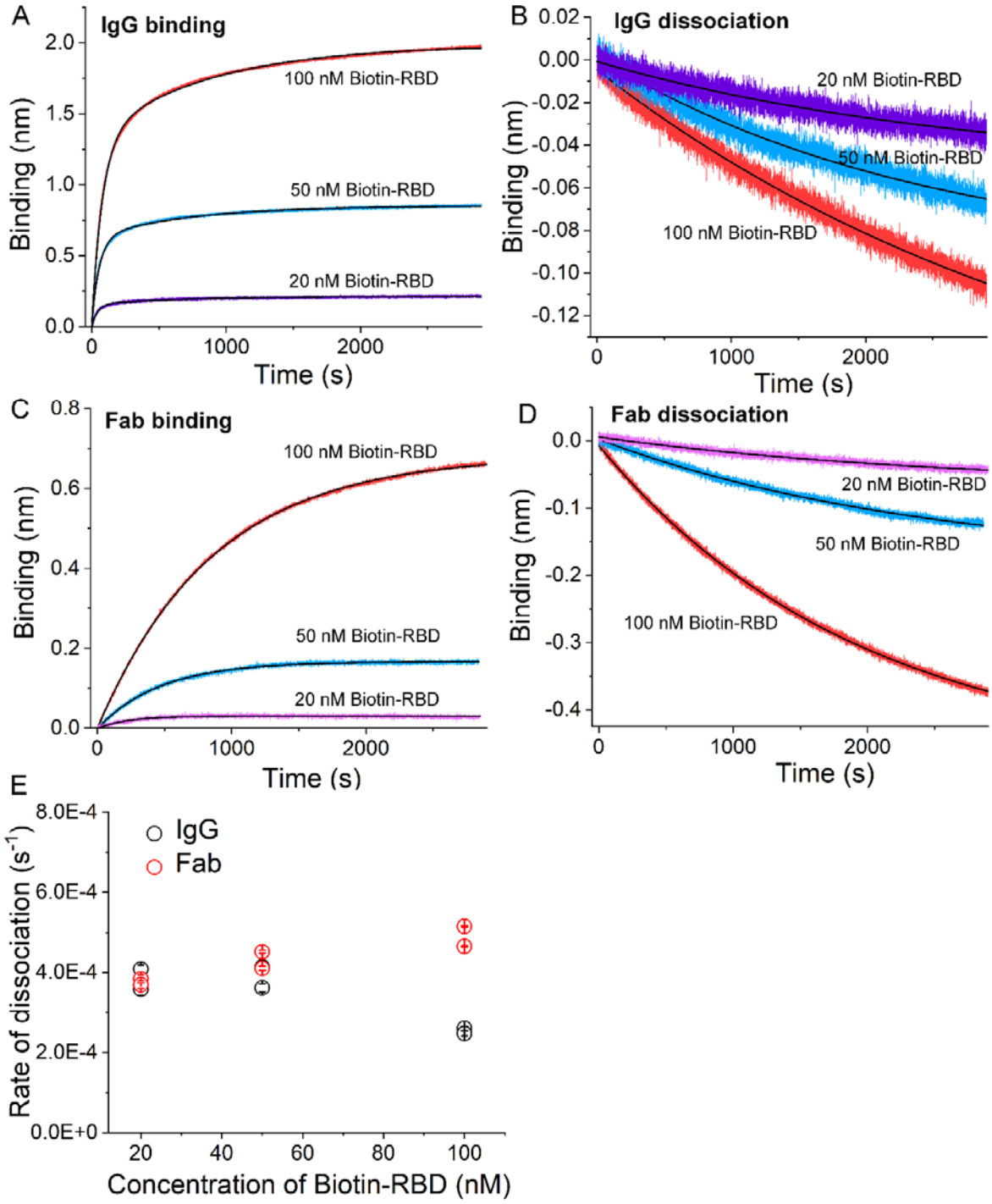

(**A**)(**B**) Real-time binding for mAb1 to biotin-RBD and its dissociation measured using BioLayer interferometry, in which mAb1 is a commercial monoclonal IgG2a specific for SARS-CoV-2 RBD (BioLegend #944803). The streptavidin sensor was coated initially with home-made biotin-RBD at three different concentrations, 20, 50 and 100 nM, as indicated inside each figure panel. The concentration of the IgG was 38 nM. (**C**)(**D**) Real-time binding for a Fab fragment to biotin-RBD and its dissociation measured using BioLayer

interferometry. The Fab fragment was prepared from mAb1 as described in Fig. S1. The streptavidin sensor was coated initially with home-made biotin-RBD at three different concentrations, 20, 50 and 100 nM, as indicated inside each figure panel. The concentration of the Fab was 62 nM. (A) through (D), the solid black lines were fits to both the binding and dissociation curves using exponential functions. Specifically, all the dissociation curves could be well described with single-exponential function and the exponent returned the rate constant of dissociation. (E) The rate constant of dissociation was plotted as a function of the concentration of biotin-RBD that was used to coat streptavidin sensors. The rate constants for IgG was shown in black circles while the rate constants for the corresponding Fab was shown in red circles. The rate constants from two independent repeats of the same experiments were plotted for both IgG and Fab, respectively. For the rate constants of IgG dissociation from streptavidin sensor of three different coating densities, a one-way ANOVA test returned a p-value of 0.03428, demonstrating that at the 0.05 level, the population means are significantly different. Specifically, the rate of dissociation from the 100-nM biotin-RBD surface was lower than that of either 20 nM or 50 nM biotin-RBD surface. This result is consistent with bivalent binding by IgG on streptavidin sensors coated with 100-nM biotin-RBD, but not for the other two conditions. For the rate constants of Fab dissociation from streptavidin sensor of three different coating densities, a one-way ANOVA test returned a p-value of 0.05601, demonstrating that at the 0.05 level, the population means are not significantly different. Specifically, the rate of dissociation from the 100-nM biotin-RBD surface was statistically indistinguishable from that of either 20 nM or 50 nM biotin-RBD surface. This result is consistent with monovalent binding by Fab on the streptavidin sensor throughout all three coating conditions. Furthermore, a one-way ANOVA test on the following 5 sets of rates of dissociation returned a p-value of 0.06043: IgG dissociation from sensors coated with 20 nM biotin-RBD, IgG dissociation from sensors coated with 50 nM biotin-RBD, Fab dissociation from sensors coated with 20 nM biotin-RBD, Fab dissociation from sensors coated with 50 nM biotin-RBD, and Fab dissociation from sensors coated with 100 nM biotin-RBD. This shows that at the 0.05 level, none of these rate constants are significantly different from one another, and thus demonstrates that IgG binds to sensors coated with either 20 or 50 nM biotin-RBD in a monovalent manner. As a consequence, we have chosen 50 nM biotin-RBD for all BioLayer interferometry experiments.

Fig. S8. Indicator of affinity maturation that is largely independent of sera IgG concentrations.

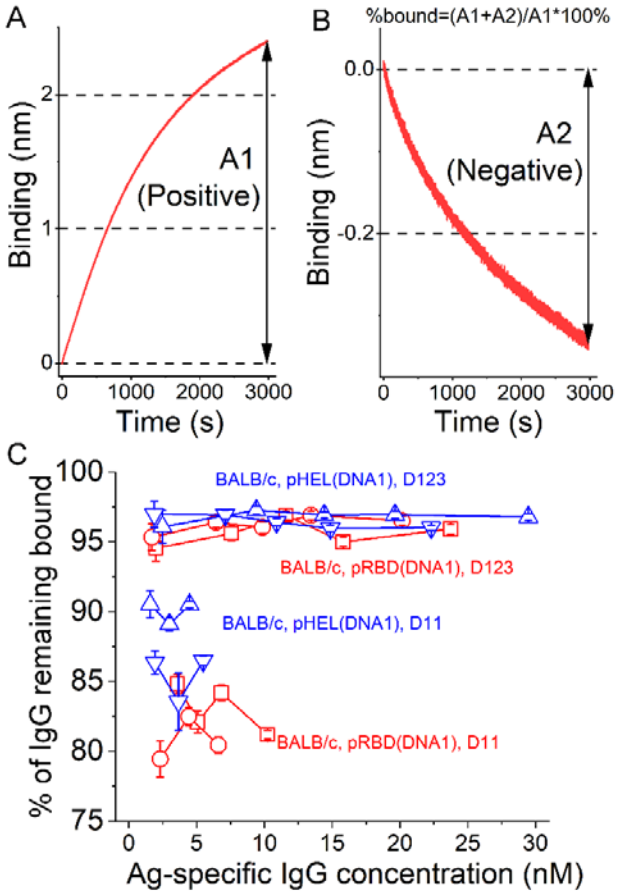

(**A**) A representative of sera IgG binding curve showing the definition of binding amplitude, A1, that is measured from BioLayer interferometry experiments. A1 is the difference in the binding signal between the end and the beginning of a binding curve, which takes a positive value with a unit of nm. (**B**) The corresponding dissociation curve from (A) showing the definition of dissociation amplitude, A2, that is measured from BioLayer interferometry experiments. A2 is the difference in the binding signal between the end and the beginning of a dissociation curve, which takes a negative value with a unit of nm. The percentage of IgG remaining bound at the end of dissociation is calculated as indicated on top of panel (B). (**C**) The percentage of IgG that remains bound at the end of dissociation was plotted as a function of the Ag-specific IgG concentration. For each color and symbol, the different concentrations were realized by dilution of the sera and then BioLayer interferometry experiments were conducted. This was done for several serum samples from BALB/c mice immunized with the agents as noted in the figure. Specifically, red squares, red circles, upper triangles, and down triangles are for pRBD(DNA1)3, pRBD(DNA1)4, pHEL(DNA1)1, and pHEL(DNA1)2, respectively. The dose of RBD was 0.24 µg per animal and the dose of HEL was 0.1 µg per animal. The concentrations for Ag-specific IgG were determined using magnetic beads capture as described in Materials and Methods.

Fig. S9. A representative standard curve from quantitative western blots to determine the concentration of Ag-specific IgG in mouse sera.

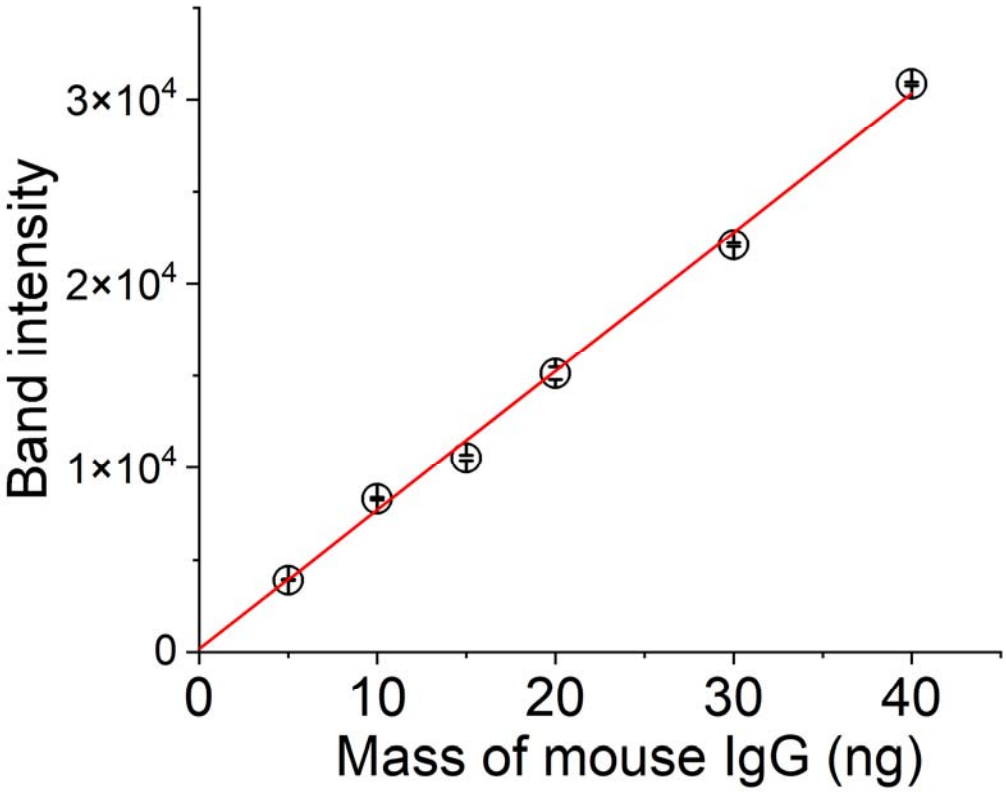

We used mAb1, the commercial monoclonal mouse IgG (BioLegend CAT#944803) as the known reference to construct a standard curve on the same western blot on which Ag-specific IgG antibodies captured by streptavidin magnetic beads were loaded. The band intensity was quantified using ImageJ and plotted against the loaded references. A linear regression (the straight red line) was then used to quantitate the mass of Ag-specific IgG in serum samples. The adjusted R-square value from the linear regression as shown above is 0.998. The mass was then used to calculate the concentration of the IgG based on volume dilutions.

Table S1. List of SVLS used in current study, together with the respective epitope density (ED), and the average number of internal nucleic acid (iNA) molecules per structure.

S1A:

Name of SVLS	ED*	# of iNA per SVLS
pRBD1	8±2	0
pRBD2	17±2	0
pRBD3	42±3	0
pRBD4	131±9	0
pRBD(DNA1)1	6±1	135±3
pRBD(DNA1)2	18±2	140±4
pRBD(DNA1)3	32±2	152±5
pRBD(DNA1)4	46±2	139±3
pRBD(DNA2)	51±3	138±3
pRBD(RNA1)	55±2	147±4

S1B:

Name of SVLS	ED*	# of iNA per SVLS
pHEL1	15±2	0
pHEL2	25±2	0
pHEL3	86±4	0
pHEL4	335±17	0
pHEL(DNA1)1	5±1	118±3
pHEL(DNA1)2	9±2	128±3
pHEL(DNA1)3	20±2	136±4
pHEL(DNA1)4	50±2	130±3
pHEL(DNA2)	47±2	126±4
pHEL(RNA1)	56±3	135±4

(A) RBD-conjugated SVLS and **(B)** HEL-conjugated SVLS. Throughout, the epitope density (ED) refers to the number of antigenic molecules specifically attached to the SVLS surface through maleimide chemistry. The # of iNA per SVLS refers to the average number of nucleic acid molecules encapsulated inside each SVLS. The uncertainties shown for both ED and iNA are standard errors determined from three independent repeats of the same ensemble experiment. Besides the above SVLS used in this study, control SVLS were SVLS that did not have any protein conjugation on surface nor have any iNA encapsulated inside SVLS.

Table S2. Statistical comparison of the titer values between SVLS(DNA1) and respective Ag-Qβ conjugates in wtB6 mice.

S2A:

	pRBD(DNA1)1	pRBD(DNA1)2	pRBD(DNA1)3	pRBD(DNA1)4
Qβ-RBD, D5	0.356	0.537	0.024	1.06e-8
Qβ-RBD, D11	2.88e-8	0.024	0.134	N.A.*

Based on the titer values that we measured for pRBD(DNA1) of varied ED and Qβ-RBD (Fig. 3B), we conducted a one-way ANOVA to test the null hypothesis that the means of titers are equal. The resulting p-values from these tests are reported in Table S2A above. At the 0.05 level, the titer for Qβ-RBD on D5 was not statistically different from that of pRBD(DNA1)1 or pRBD(DNA1)2, and was significantly lower than that of pRBD(DNA1)3 or pRBD(DNA1)4. On D11, the titer for Qβ-RBD was statistically higher than that of pRBD(DNA1)1 or pRBD(DNA1)2, and was not statistically different from that of pRBD(DNA1)3 or pRBD(DNA1)4.

*N.A. the titer values for Qβ-RBD and those from pRBD(DNA1)4 were identical within error.

S2B:

	pHEL(DNA1)1	pHEL(DNA1)2	pHEL(DNA1)3	pHEL(DNA1)4
Qβ-HEL, D5	0.207	0.537	1	1
Qβ-HEL, D11	0.134	0.356	0.356	0.356

Based on the titer values that we measured for pHEL(DNA1) of varied ED and Qβ-HEL (Fig. 3D), we conducted a one-way ANOVA to test the null hypothesis that the means of titers are equal. The resulting p-values from these tests are reported in Table S2B above. At the 0.05 level, the titer for Qβ-HEL on D5 was not statistically different from that of pHEL(DNA1)1, pHEL(DNA1)2, pHEL(DNA1)3 or pHEL(DNA1)4. Similarly, on D11, the titer for Qβ-HEL was not statistically different from that of pHEL(DNA1)1, pHEL(DNA1)2, pHEL(DNA1)3 or pHEL(DNA1)4, either.

Table S3. Statistical comparison of the titer values for SVLS(DNA1) of respective ED between wtB6 and BALB/c mice.

S3A:

	pRBD(DNA1)1	pRBD(DNA1)2	pRBD(DNA1)3	pRBD(DNA1)4
BALB/c, D5	0.356	0.537	0.356	0.134
BALB/c, D11	0.537	0.537	0.134	0.356

Based on the titer values that we measured for pRBD(DNA1) of varied ED in both wtB6 and BALB/c mice (Fig. 3), we conducted a one-way ANOVA to test the null hypothesis that the means of titer values are equal at each respective ED between wtB6 and BALB/c mice. The resulting p-values from these tests are reported in Table S3A above. At the 0.05 level, for each pRBD(DNA1), the titer values from wtB6 mice on D5 or D11 were not statistically different from those in BALB/c mice.

S3B:

	pHEL(DNA1)1	pHEL(DNA1)2	pHEL(DNA1)3	pHEL(DNA1)4
BALB/c, D5	0.537	0.537	0.356	0.356
BALB/c, D11	0.537	0.022	1.408e-8	0.022

Based on the titer values that we measured for pHEL(DNA1) of varied ED in both wtB6 and BALB/c mice (Fig. 3), we conducted a one-way ANOVA to test the null hypothesis that the means of titer values are equal at each respective ED between wtB6 and BALB/c mice. The resulting p-values from these tests are reported in Table S3B above. At the 0.05 level, for each pHEL(DNA1), the titer values from wtB6 mice on D5 were not statistically different from those in BALB/c mice. For pHEL(DNA1)1, the titer values from wtB6 mice on D11 were not statistically different from those in BALB/c mice. However, for pHEL(DNA1)2, pHEL(DNA1)3 and pHEL(DNA1)4, the titer values from BALB/c mice on D11 were statistically higher than those from wtB6 mice.

Table S4. Statistical comparison of the IgG1 ELISA OD450 values for pRBD(DNA1) of respective ED between wtB6 and BALB/c mice.

	pRBD(DNA1)1	pRBD(DNA1)2	pRBD(DNA1)3	pRBD(DNA1)4
BALB/c, D5	0.512	0.075	0.043	0.609
BALB/c, D11	0.085	0.047	0.444	0.940

Based on the IgG1 ELISA OD450 values that we measured for pRBD(DNA1) of varied ED in both wtB6 and BALB/c mice (Fig. 4A and Fig. S5A), we conducted a one-way ANOVA to test the null hypothesis that the means of ELISA OD450 values are equal at each respective ED between wtB6 and BALB/c mice. The resulting p-values from these tests are reported in Table S4 above. At the 0.05 level, the majority of ELISA OD450 values from wtB6 mice on D5 or D11 were not statistically different from those in BALB/c mice, except pRBD(DNA1)3 on D5 and pRBD(DNA1)2 on D11, where higher IgG1 levels were observed in BALB/c mice.

Table S5. A summary of key findings from the current study regarding mechanisms of a nAb response in mice upon a primary encounter with virus-like Ags and their implications for understanding viral immunogenicity.

Neutralizing antibody response →

SVLS type	Mouse strains	Initiation (by Day 5)	Amplification (by Day 11)	Duration (Day 12 to 300+)
High ED, no iNA 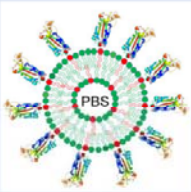	B6	Yes	Yes, but limited compared to BALB/c	Wane with time
		IgG1 IgG2b IgG3 T-cell independent CD19 dependent, MyD88 independent		
	BALB/c	Yes	Yes, with strong IgG1	Grow with time
		IgG1 IgG2b IgG3		
Low ED, with iNA 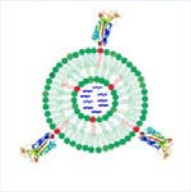	B6	Yes	Yes	Wane with time, but a stronger response than SVLS without iNA
		IgG1 IgG2b IgG2c IgG3 T-cell independent Can be CD19 independent, TLR/MyD88 dependent		
	BALB/c	Yes	Yes	Grow with time, and a stronger response than SVLS without iNA
		IgG1 IgG2a IgG2b IgG3		

Based on current studies, we divide the time dependence of a nAb response into three segments: initiation (by D5), amplification (by D12) and duration (D12 to 300 and beyond). Both SVLS with high ED but without iNA and SVLS with low ED and iNA can induce nAb responses in either B6 or BALB/c mice, although the details in terms of initiation, amplification and duration are different. For SVLS of high ED but without iNA, they initiate a nAb response in B6 mice and the animals produce IgG1, IgG2b and IgG3, like that in BALB/c mice, but the amplification of the nAb response is limited compared to that in BALB/c mice. The nAb level also wanes with time, which contrasts with the nAb response in BALB/c mice that grows with time. BALB/c mice has more IgG1 produced during the stage of amplification. These nAb responses in B6 mice are largely T-cell independent and MyD88 independent but depend on CD19 as revealed by experiments in gene knockout mice of B6 background. For SVLS of low ED with iNA, they initiate nAb responses in both B6 and BALB/c mice and the animals produce IgG1, IgG2c/2a, IgG2b and IgG3. Both the initiation and amplification are similar in these two strains of mice, although the durations are different. The nAb response wanes with time in B6 mice but grows with time in BALB/c mice. For both strains, the nAb responses are much stronger than the responses induced by SVLS without iNA. These nAb responses in B6 mice depend on TLRs and MyD88 but are largely T-cell independent and can be even mounted in the absence of CD19 as revealed by experiments in gene knockout mice of B6 background. In conclusion, the minimum biochemical constituents required to initiate a nAb response are a foreign protein and lipids. Ag-specific B cells integrate both features of viral signals, i.e., ED and iNA, from individual

viral particulate Ags to initiate a nAb response. The intrinsic sensing of iNA by TRLS is critical for both short and long terms of the Ab response.

The mechanism by which nAbs are produced explains key features of the nAb response in live viral infections, including its speed (*29*), the type of nAb class switch, and the T cell independence of the immediate but potent nAb response (*28, 60, 75-77*) that does not require somatic hypermutation or affinity maturation (*94*).

Lastly, it is important to note that the potency of secreted IgG to neutralize viruses can be affected by ED from the perspective of IgG binding avidity. While low ED on the surface of SVLS with iNA can activate antigen-specific B cells and lead to strong IgG secretion, low ED on the surface of virions can also adversely affect the neutralization potency of the secreted IgG (*2*). This is because a low ED on virion surfaces can impede the bivalent binding of IgG, thereby reducing binding avidity, as has been demonstrated for HIV-1 (*97*).